Solid Earth Discuss., https://doi.org/10.5194/se-2017-130
Manuscript under review for journal Solid Earth
Discussion started: 14 December 2017

High stresses stored in fault zones : example of the Nojima fault (Japan)

Anne-Marie Boullier[1], Odile Robach[2], Benoît Ildefonse[3], Fabrice Barou[3], David Mainprice[3], Tomoyuki Ohtani[4], Koichiro Fujimoto[5]

[1]ISTerre, Univ. Grenoble Alpes, CNRS, 38000 Grenoble, France
[2]CEA, INAC-MEM, Univ. Grenoble Alpes, 38000 Grenoble, France
[3]Géosciences Montpellier, CNRS, Univ. Montpellier, 34095 Montpellier, France
[4]Gifu University, Department of Civil Engineering, Gifu 501-1193, Japan
[5]Faculty of Education, Tokyo Gakugei University, Tokyo, Japan

Correspondence to: Anne-Marie Boullier (anne-marie.boullier@univ-grenoble-alpes.fr)

Abstract. During the last decade pulverized rocks have been described on outcrops along large active faults and attributed to damage related to a propagating seismic rupture front. Questions remain on the maximal lateral distance from the fault plane and maximal depth for dynamic damage to be imprinted in rocks. In order to document these questions, a core sample of granodiorite located at 51.3 m from the Nojima fault (Japan) that was drilled after the Hyogo-ken Nanbu (Kobe) earthquake is studied by using Electron Back-Scattered Diffraction (EBSD) and high resolution X-ray Laue microdiffraction. Although located outside of the Nojima damage fault zone and macroscopically undeformed, the sample shows pervasive microfractures and local fragmentation that are attributed to the first stage of seismic activity along the Nojima fault characterized by laumontite as the main sealing mineral. EBSD mapping was used in order to characterize the crystallographic orientation and deformation microstructures in the sample, and X-ray microdiffraction to measure elastic strain and residual stresses in a quartz grain. Both methods give consistent results on the crystallographic orientation and show small and short wave-length misorientations associated with laumontite-sealed microfractures and alignments of tiny fluid inclusions. Deformation microstructures in quartz are symptomatic of the semi-brittle faulting regime, in which low temperature brittle, plastic deformation and stress-driven dissolution-deposition processes occur conjointly.

Residual stresses are calculated from elastic strain measured by X-ray Laue microdiffraction and stress peaks at 100 MPa (mean 141 MPa). Such stress values are comparable to the peak strength of a damaged granodiorite from the damage zone of the Nojima fault indicating that, although apparently macroscopically undeformed, the sample is actually highly damaged. The homogeneously distributed microfracturing of quartz is the microscopically visible imprint of this damage and suggests that high stresses were stored in the whole sample and not only concentrated on some crystal defects. It is proposed that the high residual stresses are the sum of the stress fields associated with individual dislocations, dislocation microstructures and originated from the dynamic damage related to the propagation of rupture fronts or seismic waves associated to M6 to M7 earthquakes during Paleocene on the Nojima fault at a 3.7 – 11.1 km depth (laumontite stability domain) where confining pressure prevented pulverization. The high residual stresses and the deformation microstructures

would have contributed to the widening of the damaged fault zone with additional large earthquakes occurring on the Nojima fault.

1 Introduction

Using near-field seismic data recorded during earthquakes, it is possible to derive kinematic rupture models describing the spatial distribution of slip, rupture time and rise-time on the fault. Inversion of such models allows the determination of the space-time history of shear stress on the fault plane during the rupture. As an example, dynamic shear stress drop calculated for four well-instrumented large earthquakes on the San Andreas fault system varies from 20 MPa to 100 MPa (Bouchon, 1997). These values are very heterogeneous along the fault plane and can be regarded as a lower bound because of the limited spatial resolution of the kinematic models, which is at best a few kilometers. If the shear stress drop may be evaluated, the pre-earthquake and the residual stress levels need to be measured in-situ in deep wells and boreholes by hydraulic fracturing technique and analysis of stress-induced well bore breakouts (Zoback and Healy, 1992) or by anelastic strain recovery measurements on cores retrieved from boreholes (Lin et al., 2006). For example, differential stress measured in the SAFOD pilot hole are ≈60 MPa at 1671m depth (Hickman and Zoback, 2004). This value is considerably lower than the up to 300 MPa residual stress measured by Chen et al. (2015) in quartz fragments within the damage zone of the San Andreas fault at 2.7 km depth (*ca* 100 MPa confining pressure) using X-ray Laue microdiffraction. This is the unique residual stress value available in a damaged fault zone.

Considering this high level of residual stress, large damage is expected in rocks surrounding a fault. Actually, when earthquake occurs, displacement is localized on a very thin (<10 mm) slip zone (Chester and Chester, 1998 ; Sibson, 2003) in which a gouge is formed by friction-related grain-size reduction (Sibson, 1977). Outside the fault core, 1 to 10^3 m wide zones may be damaged by brittle failure of the surrounding rocks. Recently, several examples of pulverized rocks lacking significant shear have been described at the surface or subsurface within 100 to 200 m wide bands close to large faults such as the San Andreas fault (Dor et al., 2006 ; Rockwell et al., 2009; Wechsler et al., 2011) or the Arima-Takatsuki Line in Japan (Mitchell et al., 2011), and have been attributed to dynamic co-seismic damage. At the same time, high strain-rate experiments on granite using Hopkinson bars without confinement have reproduced similar pulverized rocks (Xia et al., 2008) and predicted a dynamic shear stress threshold for pulverization (Doan and Gary, 2009). Below the pulverization threshold, fractures without shear are formed in the samples, which remain cohesive. Yuan et al. (2011) have performed similar experiments under confinement and did not observe pulverization under 132 MPa, which was the maximum confining pressure allowed by their apparatus. They suggest, therefore, that co-seismic pulverization process is restricted to the uppermost crust (≤ 3 km or ~100 MPa confining pressure). Actually and until now, pulverized rocks have been mostly observed at shallow levels although a few cases of co-seismic damage at depth are documented in the literature. Fragmentation of garnet at very high stresses and strain rates at depth corresponding to temperatures of about 300-350°C was first described by Trepmann and Stöckert (2002) in the Sesia Zone (Italian Alps). More recently, garnet fragmentation associated to pseudotachylites in the Western Norway eclogitic crust was attributed to deep crustal earthquakes (Austrheim et al., 2017). Concerning carbonate lithologies, Sagy and Korngreen (2012) described pulverized rocks in a deep borehole at 5 km depth in Israel.

In this paper, we will investigate the natural deformation microstructures of a sample located in the vicinity of the Nojima fault (Japan). The studied sample was deformed at 4-11 km depth during a first period of seismic activity on the Nojima fault dated from *ca* 56 Ma ago, then brought to near surface by uplift and erosion and collected at 220 m depth by the Geological Survey of Japan in the Hirabayasdhi drillhole. We will compare the deformation microstructures of that sample with experimentally produced microstructures during dynamic loading and with naturally fragmented fault rocks described in the literature. For microstructural observations, techniques of petrographic microscopy, Scanning Electron Microscopy (SEM), cathodoluminescence (CL), Electron Back Skattered Diffraction (EBSD) and X-ray Laue microdiffraction were used to characterize microfractures, their cement and the intragranular heterogeneities of crystallographic orientation in quartz grains, and to map the elastic strains and residual stresses as Chen et al. (2015) have done for a sample of the San Andreas fault zone. We will discuss the significance of the results in terms of stress and strain-rate and the contribution of the observed microscopic damage to the widening of the damaged fault zone.

2 Geological setting

The Nojima Fault is a N45°-striking and 85° SE-dipping dextral reverse fault (Fig. 1a) on which occurred the 1995 Hyogo-ken Nanbu earthquake (Kobe earthquake, M 7.2). The fault cuts across the Cretaceous Ryoke granodiorite. One year after the earthquake the Geological Survey of Japan (GSJ) successfully drilled the Hirabayashi borehole through the Nojima Fault on Awaji Island. Cores were recovered for almost entire depth interval from 150 to 746.6 m due to the cohesion the rocks (Ito et al., 2000). The drillhole sampled the Principal Slip Zone (PSZ) of the Kobe earthquake at 624.5 m depth (Fig. 1b; Ohtani et al., 2000a; Tanaka et al., 2001). Two major periods of seismic activity on the fault separated by an exhumation of the basement of the Awaji Island were inferred using the relationships between hydrothermal minerals and deformation microstructures (Boullier et al., 2004a). The first period of seismic activity was characterized by pseudotachylites and by laumontite as the main sealing mineral. Laumontite is a zeolite ($Ca_4(Al_8Si_{16}O_{48})\cdot 18H_2O$) which crystallizes from aqueous fluids in the 100-300 MPa pressure range and at temperature lower than 300°C (Cho et al., 1987), which fixes the depth range of laumontite precipitation and laumontite-associated deformation to a 3.7 to 11.1 km depth interval using a rock density of 2.7 g/cm^3 and a lithostatic pressure gradient. This first period of seismic activity has been dated around 56 Ma by fission tracks in zircon (Murakami and Tagami, 2004). The second period (≤ 1.2 Ma) was characterized by carbonates precipitating in co-seismic fractures (Boullier et al., 2004b) and the composition is consistent with the fluids circulating within the fault to day (Fujimoto et al., 2007). This two-stage tectonic history of the Nojima fault is compatible with the regional structural analysis (Kanaori, 1990 ; Fabbri et al., 2004 ; Famin et al., 2014), which reveals a sinistral wrenching in the Paleogene (65 to 23 Ma), followed by fault-normal extension in the Miocene (23 to 6 Ma) and a dextral slip active since the Plio-Quaternary (≤ 2 Ma). In the present paper, we focus on deformation microstructures formed during the first period of seismic activity in a sample, which was in the 3.7 - 11.1 km depth range as constrained by the laumontite stability field before being exhumed and sampled at 220 m depth by the GSJ drillhole. By comparing conductive planes detected by the Fullbore Formation MicroImager (FMI, trademark of Schlumberger) with open fractures on 360° azimuthal core scanner images, it was possible to reorient most sections of the drillcore (Ohtani et al., 2000b). Therefore, microstructures observed in the studied sample could be geographically oriented, which is not usually the case.

3 Analytical procedures

3.1 EBSD

Small-scale observations were performed on polished thin (100 µm thick) sections cut perpendicular to the drill-core axis, *i.e.* close to the horizontal plane. Examination with a petrographic microscope was used to recognize the characteristic microstructural features and sealing minerals.

Crystallographic orientation of quartz was determined by indexation of electron-backscattered diffraction (EBSD) patterns using the Camscan Crystal Probe X500FE SEM (Géosciences Montpellier, CNRS, Université de Montpellier), equiped with EBSD HKL NordlysNano detector for crystallographic analysis and an EDS X-Max^N 20mm² detector for chemical analysis, both being driven by the AZtec software (Oxford Instruments). Diffraction patterns were generated at 20° tilted incident electron beam with a horizontal carefully polished thin section (note this equivalent to 70° tilt of conventional SEM). The orientation maps were obtained in automatic acquisition mode with a step size of 4µm or 0.5µm for detailed areas. Standard post-acquisition data processing was done using the Tango software of the Channel 5® suite (HKL Technology), to (i) remove isolated pixels that are indexed as a given phase and surrounded by either non-indexed pixels of pixels indexed for another phase, and (ii) fill non-indexed pixels that have a minimum of 6 neighbouring pixels with the same orientation, EBSD data processing was then performed using the MTEX open source matlab toolbox (version 4.3.1; http: //mtex-toolbox.github.io/; Hielscher and Schaeben, 2008; Bachmann et al., 2010: Mainprice et al., 2014).

3.2 Laue X-ray microdiffraction

Laue X-ray microdiffraction maps were collected on the same thin section as for EBSD using the synchrotron X-rays of a bending-magnet at the ESRF (Grenoble) and the apparatus of the CEA-CNRS CRG-IF BM32 beamline following a method described by Ulrich et al. (2011) and Robach et al. (2017). The 0.5 x 0.5 µm^2 polychromatic (5 to 22 KeV) horizontal X-ray beam impinges the sample surface inclined at 40° angle (Figure 2a). The Laue patterns were collected on a MAR 165 CCD camera with 165 mm diameter and 2048 x 2048 pixels at 70 mm to the sample (Figure 2b), mounted around a diffraction angle 2θ of 90° (in reflection geometry). The geometry of the diffraction experiment was calibrated using the Laue pattern of a Ge single crystal, as described in Ulrich et al (2011). The sample was scanned in front of the X-ray microbeam for mapping using a high-resolution x-y stage. Exposure time at each x-y point was 0.2s. The probing depth in the investigated X-ray transparent material (quartz) is limited by the thickness (100 μm) of the thin section. Depending on the (x, y) position of the probe, quartz deformation, single spots (one cristallite) or multiple spots (several subgrains) are obtained (Figure 2c). Automated analysis of Laue patterns comprises different stages that were described in Tamura (2014) for XMAS software and Robach (2017) for LaueTools software (Micha et al., http://sourceforge.net/projects/lauetools/). Here LaueTools software was used for the Laue pattern indexation, determination of the crystal Euler angles (orientation) and the distorsion of the quartz unit cell (elastic strain, obtained by comparing the experimental and the undeformed unit cell). The details of the data analysis are explained in the Appendix A.

4 Characterization of microstructures

The NOJ220 sample studied in this paper is a macroscopically undeformed granodiorite located outside the damage fault-zone at 220m depth in the borehole and a distance d_{fault} = 51.3 m to the fault plane in the hanging-wall (see Fig. 1b). It shows a typical isotropic magmatic structure characterized by large euhedral orthose and plagioclase (up to 43% anorthite), hornblende and biotite crystals, which appear as gray, green and brown respectively on the thin section (Figure 3a), by cm-size quartz and by accessory minerals such as zircon, apatite, titanite and allanite. Deformation microstructures are nevertheless omnipresent when observed under the microscope. They are described below.

4.1 Laumontite-filled veins

Two types of laumontite-filled veins are defined depending on their size. The first type is represented by wide (up to 1mm) and long (more than 3 cm, the thin section length) veins, which are indicated by yellow arrows on Figure 3a. They are generally straight or slightly curved, and E-W striking and 70° southward dipping in the geographic frame. They contain large angular fragments of the granodiorite minerals embedded in small (<0.2 mm) laumontite crystals (Figure 3b and 3c). Fragments generally do not touch each other. Biotite fragments are delaminated, as are some biotite crystals immediately adjacent to the veins. The different nature and crystallographic orientation of the fragments compared to the fracture-wall minerals suggest that these fragments have been at least rotated and probably transported some distance from their initial position. The widest veins are clearly dilatant with some shearing component as shown by the deformed cleavages of neighbouring biotite crystals. However, the exact opening kinematics cannot be clearly established on the basis of the horizontal thin section alone. They may be qualified as "breccia-like" veins and are similar to those described by Blenkinsop and Sibson (1992, their fig. 4d) in the core samples from the Cajon Pass drillhole near to the San Andreas Fault.

The second type is represented by 20 – 200 μm wide and several cm long veins. They are transgranular, straight or with a jigsaw geometry, which are roughly E-W orientated and filled by laumontite prisms. They do not contain fragments and have parallel vein walls (thick black arrows on Figure 4b; Si, Ca and Al maps in Figure 4e). In these veins, the prisms of laumontite are generally orientated at high angle to the vein walls.

4.2 Deformation microstructures in quartz

When observed under the petrographic microscope, quartz grains display an intracrystalline deformation characterized by undulous extinction without dynamic recrystallization. They are also pervasively affected by numerous intragranular N50° orientated microfractures (Figure 4a), which are only visible at a small scale (small black arrows in the grain investigated using EBSD, Figure 4b) and are sealed by laumontite as shown on the Si, Ca and Al maps on Figure 4e. Nevertheless, quartz grains have preserved their magmatic shape (Figure 3a), thus indicating a low finite strain.

Fluid inclusions in quartz grains of the NOJ220 sample are unusual. Contrary to fluid inclusions in undeformed quartz-bearing rocks which have generally rounded or negative crystal shapes (Roedder, 1984), fluid inclusions define short (tens of μm) alignments of tiny neonate fluid inclusions (see Figure S1). These alignments share the same N50° orientation parallel to the Nojima fault in all quartz grains independantly of the crystallographic orientation of the host quartz (Figure S1a). They form a continuum with the pervasive intragranular N50°-orientated healed microfractures, which share the same dark blue signature on the SEM-cathodoluminescence image and are themselves branched on laumontite-filled veins (see Figure S2). The alignments of tiny fluid inclusions are present in all the core samples within the 200 m to 750 m depth range in the GSJ drillhole.

4.3 Kink-bands in biotites

Kinking of (001) cleavage in biotite is a common feature in the NOJ220 sample as in all samples along the drillhole. Kink-bands are at a high angle to (001) cleavage and are comparable to kink-bands in granitic samples from the shock region around a nuclear explosion (Cummings, 1965 ; Fauré, 1970). They provide a marker to extract the shortening intensity by measurement of the change in length of (001) cleavages, and the direction of compression by measuring the orientation of kink-bands (Figure S1b). Strain recorded by biotite in the NOJ220 sample reaches up to 5% and kink-bands are roughly N50° orientated parallel to the alignments of tiny fluid inclusions described above (Figure S1a) and to the Nojima fault.

5 EBSD measurements in quartz

The quartz grain investigated using EBSD (Figure 4) is representative of the average density of microfractures in the NOJ220 sample. The misorientation map (*i.e.* misorientation of each pixel relative to the mean orientation of the grain; Figure 5b) shows a chessboard pattern defined by large (50-100 μm) subgrains limited by sharp boundaries which are mostly independant of the microfracture geometry. Smaller misorientation domains are superimposed on this chessboard pattern and are roughly elongated parallel to the microfractures (lower right area in Figure 5b), but are cross-cut by them in many places. Misorientation axes for subgrain (either large or small) boundaries showing 0.5° to 5° misorientation are preferentially around the (0001) axis (Figure 5d). Dauphiné twinning characterized by a rotation of 60° around (0001) is shown on the map of Inverse Pole Figures of the X axis (IPF X, Figure 5a) by the small dark green domains and on the pole figures (Figure 5c) by the superposition of (10-11) and (01-11) in twinned and untwinned domains when (11-20) and (10-10) remain the same (*e.g.* Mainprice et al., 1993). Note that the Dauphiné twinned domains are also slightly elongated in N50° direction similar to that of the intragranular microfractures.

Microfractures may be locally very dense as in the N50° to N90° orientated array joining one biotite or hornblende to another across the whole thin section (Figure 6). Figure 7 shows a quartz grain of this array which is squeezed in between a biotite and an amphibole, and cut by numerous microfractures radiating in a Hertzian pattern and sealed by laumontite (Ca, Al and Si maps in Figure 7c). Up to 30% dilatancy was measured on the SEM image (Figure 7b) by cumulating the thicknesses of laumontite-filled microfractures on a transect perpendicular to them. Alignments of tiny fluid inclusions in the neighbouring quartz have a strong N50° orientation and display the same dark-blue cathodoluminescence signature as the healed microfractures which are themselves in continuity with the laumontite-sealed microfractures (see Figure S3). Only the quartz grains were selected for the EBSD map. EBSD measurements of the three quartz grains reveal Dauphiné-twinned domains (Figure 8a) showing the same crystallographic relationships as in the previous example (see pole figures in Figure 8c), and misorientation domains (Figure 8b). As for the quartz grain investigated in Figure 5, large subgrains define a chess-board pattern independent of the microfracture geometry. Superimposed smaller misorientation domains are roughly elongated parallel to, but cross-cut by the microfractures. Misorientation angle relative to the mean reaches up to 10° (Figure 8b) compared to the 5° misorientation in the mildly microfractured quartz mapped in Figure 5b. Rotation axis of subgrain boundaries showing >0.5° misorientation is again preferentially around [0001] (Figure 8d). However, pole figures (Figure 8c) do not show significant dispersion of crystallographic axes around [0001]. The three components of rotation (Rx, Ry and Rz) were calculated using the EBSD data and the Laue Tools Package (Figure 9, see Supplementary Material 4 for mathematical transformations applied to the EBSD data in order to pass the orientation matrices and map points positions into the LaueTools sample reference frame). They indicate that neighbouring fragments did not rotate greatly relative to each other (2° to 5°) during fragmentation. Actually, Rx component (max. 30 mrad or 1.72°) is slightly lower than Ry (max. 64 mrad or 3.67°) and Rz (max. 90 mrad or 5.15°).

6 Elastic strain and residual stress

In order to characterize the small misorientation domains and the damage related to microfracturing, a small area of the representative quartz grain studied in Figures 4 and 5 (see location on Figures 4b and 5b) was investigated in detail using EBSD and X-ray Laue microdiffraction.

6.1 Orientation map

A high resolution EBSD map was performed with a 0.5 μm step and misorientation to the mean orientation was calculated (Figure 10b). As already observed in Figure 4c and 4d, two types of intracrystalline deformation features are observed: (i) large 50 to 100 μm wide sub-grains limited by sharp straight or slightly curved sub-grain boundaries (Figure 10b) with 0.5° to 1° misorientation indicated by large steps on the misorientation profile (Figure 10c), and (ii) small elongated sub-grains within the large ones, NNE-SSW orientated and showing less than 0.3° short wave-length misorientations (Figures 10c and suppl. mat. S5) with the same order of accuracy as the EBSD measurements performed with the Crystal Probe. However, as these small elongated subgrains coincide with the healed short microfractures or the alignments of tiny fluid inclusions (arrows on Figure 10a and 10b), they are believed to be significant even if their misorientation is very small (<0.2°, see Figure S5). Misorientation axes corresponding to some of these subgrains have been determined (Figure 10d) and are close to [01-11] or [01-12].

The same area has been then analyzed by X-ray Laue microdiffraction. A high definition map with a 2.5 μm step (89 lines, 101 columns, 8989 images) was constructed on the 250 x 220 μm^2 zone. In this area, the relative simplicity of the Laue images (low number of subgrains within the analyzed volume) allows measuring the orientation and local deviatoric distorsion of the quartz unit cell with a good precision (~0.1 mrad). The crystallographic orientation was determined in each point of the map and the rotations Rx, Ry and Rz of the crystal lattice around the x, y and z axes (sample referential, see Figure 2) relative to the average orientation matrix were calculated (Figure 11a ; see Appendix A and references therein for the details of calculation and methods of data filtering).

The spatial and angular resolutions obtained with X-ray Laue microdiffraction are lower and higher, respectively, than those obtained with EBSD. However, these two technique sample different regions as EBSD samples the surface and X-ray Laue microdiffraction a volume of 1 x 1 x 100 μm^3, respectively (see Analytical Procedures). There is a good correlation between the domains indicated by Rx , Ry and Rz rotations calculated with Laue Tools Package applied on X-ray Laue microdiffraction data (Figure 11a) and on EBSD data (Figure 11b). The subgrain boundaries correspond to the misorientation maps and the misorientation angles measured with the two methods are comparable (Figure 11a and 11b). These maps also indicate that Ry misorientations are larger than Rz and Rx for both techniques. Moreover, the Ry map highlights the small-elongated subgrains parallel to the healed short microfractures or the alignments of tiny fluid inclusions.

6.2 Lattice distorsion - Elastic strain

The elastic strain measurement performed by X-ray microdiffraction is based on the slight distorsion of the experimental Laue pattern compared to the pattern of an undeformed crystal of the same orientation, *i.e.,* the angular distances between spots of the Laue patterns in the deformed crystal are compared to those of an undeformed reference pattern. The data have been filtered using two estimators of the quality of the Laue pattern refinement (number of spots and average distance between experimental and reference pattern spots, see Appendix A for explanation). It is possible to calculate the six main components of the deviatoric elastic strain tensor (ε_{XX}, ε_{YY}, $\varepsilon_{ZZ,}$ ε_{YZ}, ε_{XZ}, ε_{XY} with ($\varepsilon_{XX} + \varepsilon_{YY} + \varepsilon_{ZZ} = 0$) on each point of the map (Figure S6). Values of equivalent strain may be calculated from the strain tensor :

$$\varepsilon_{eq} = 2/3\ [(\varepsilon_{XX} - \varepsilon_{YY})^2 + (\varepsilon_{YY} - \varepsilon_{ZZ})^2 + (\varepsilon_{ZZ} - \varepsilon_{XX})^2 + 6\ (\varepsilon_{XY}{}^2 + \varepsilon_{XZ}{}^2 + \varepsilon_{YZ}{}^2\ )]^{1/2} \qquad (1)$$

and are reported without filtering (Figure 12a) or after filtering (Figure12b). Equivalent strain and the components of the elastic strain tensor (Figure S6) are roughly correlated with the microstructures revealed by EBSD (sub-grain boundaries, see Figure 10b) or with the Rx, Ry and Rz maps (Figure 11), and with microfractures as well. However, some domains with no important misorientation or subgrains such as the upper left corner on the map (Figure 11), display important elastic strain (more than 2.5 10^{-3}, Figure 12).

The distribution histograms of the equivalent strain value in each point of the map is given in Figure 13a. Without filtering equivalent strain varies up to more than 2.5 10^{-3}, but the highest values (>2.5 10^{-3}) removed by filtering. Nevertheless, mean equivalent strain after filtering is still at 0.96 10^{-3}.

6.2 Residual stresses

The distorsion of the crystal lattice measured above is purely elastic, thus the residual stress tensor may be deduced by applying the Hooke's law :

$$\sigma_{ij} = C_{ijkl}\ \varepsilon_{kl} \qquad (2)$$

where σ is the stress, ε_{kl} the elastic strain and C_{ijkl} the elastic coefficients for α-quartz as determined by Ogi et al. (2006) at 30°C. Thus, the residual stress may be calculated on each point of the map and as a consequence of the proportionality between strain and stress, the residual stress maps representing the components of the residual stress tensor are similar to the elastic strain ones. As for equivalent strain, equivalent (or von Mises) stress was calculated on each point of the map following the equation :

$$\sigma_{eq} = (1/2\ ((\sigma_{xx}-\sigma_{yy})^2 + (\sigma_{yy}-\sigma_{zz})^2 + (\sigma_{xx}-\sigma_{zz})^2 + 6\ ((\sigma_{yz})^2 + (\sigma_{xz})^2 + (\sigma_{xy})^2)))^{1/2} \qquad (3)$$

and reported as a distribution histogram (Figure 13b). The filtered von Mises stress displays a peak at 100 MPa for a mean at 141 MPa.

7 Interpretation and discussion

The NOJ220 sample studied in this paper is located at 51.3 m from the main Nojima fault, that is outside the fault zone determined on the basis of studies of the drillcore samples (Ohtani et al., 2000a; Tanaka et al., 2001). Deformation microstructures corresponding to a low strain are nevertheless present in the thin section. We discuss now the observed microstructures in terms of stress and strain-rate, *i.e.* their time of formation in relation with a seismic rupture (Figure 14), and their significance in the development of the damage zone around the Nojima fault.

7.1 Laumontite-filled veins

Two types of veins or microfractures have been defined in the NOJ220 sample. The fact that all of them are sealed by laumontite clearly indicates that they accompanied the first periode of seismic activity on the Nojima fault (Boullier et al., 2004a) around 56 Ma (Murakami and Tagami, 2004). The laumontite stability field in the 100-300 MPa pressure range (Cho et al., 1987) constrains the depth of formation of these veins at 3.7-11.1 km depth assuming a lithostatic gradient and a 2.7 g.cm^{-2} density of rocks.

What could we say on the kinetics of opening and sealing of these veins and microfractures ? In the E-W striking breccia-like veins, as pointed above, the fragments of minerals are large and angular suggesting the absence of attrition and indicating that the veins were formed in a single event of dynamic fracturing (Figure 14). The fragments were transported away from their source locality by fluid advection in the fractures at least before their complete sealing by laumontite. Thus, the opening of breccia-like veins corresponds to a single transient high permeability stage in the Nojima fault vicinity and is interpreted to have occurred during single seismic event. Fracture opening has induced post-seismic circulation of a hot fluid coming from greater depths and crystallizing laumontite during cooling (Figure 14).

The significance of the second type of veins is not so clear. The morphology of the laumontite prisms and their orientation with respect to the vein walls confirm that they are mode I opening fractures and, by comparison with numerical modelling of vein opening and sealing (Hilgers et al., 2001) suggest equal rates of vein opening and laumontite growth. These veins are E-W orientated and parallel on average to (or branched on) the breccia-like laumontite-filled veins and thus, are probably associated to them. However, they do not contain mineral fragments; this may be due either to their smaller thickness preventing the transport of fragments by the advecting fluid or to a slower rate of fracture opening. The type 2 veins and especially the dense array illustrated in Figure 6, are also very similar in shape to the experimental fractures described by Aben et al. (2016). These authors have performed successive high strain-rate loadings (180 s^{-1} to 90 s^{-1}) on granitic cylinders using Hopkinson bars below the pulverization threshold in order to simulate successive seismic events. The numerous fractures created in these experiments run roughly parallel to the loading direction and show only dilation and no shear (Aben et al., 2016). The quartz grain described in the Figure 7 and displaying fractures radiating in a Hertzian pattern may also be compared to quartz grains in damaged sandstones along the San Andreas Fault (Dor et al., 2009). By analogy, the opening of type 2 laumontite veins is tentatively attributed to a co-seismic or dynamic stage (Figure 14) although their orientation is more difficult to interpret (E-W sriking veins versus N50° striking Nojima fault). Do these veins represent one or several seismic events? Following Aben et al. (2016) additional loading led to the growth of new fractures rather than failure on the already created fractures resulting into homogeneously distributed fractures within the sample. Therefore, the sum of the veins either breccia-like or mode I that are observed in the NOJ220 sample may correspond either to several « mild » seismic events characterized by similar loading conditions or to the propagation of a single seismic rupture. The second interpretation is favoured because no clear cross-cutting are observed, but branching relationships between veins were observed. Whatever the interpretation, the consequence of coseismic fracturation is a fast and transient increase of the permeability allowing circulation of hot advecting fluids and sealing of fractures by laumontite (Figure 14).

7.2 Microfractures and alignments of tiny fluid inclusions in quartz

What are the relationships between the formation of microfractures and of the alignments of tiny fluid inclusions? As described above, the alignments of tiny fluid inclusions are well orientated at the sample scale (Boullier, 2011 ; Figure S1), independantly of the orientation of the host crystal and are parallel to the Nojima fault. Therefore, we may infer that quartz behaves as an isotropic material during the dispersion of large fluid inclusions into tiny ones and that this phenomenom is related to the macroscopic tectonic loading. Small intragranular microfractures and alignments of tiny fluid inclusions have the same cathodoluminescence signatures (Figure S2 and S3), identical to that of quartz in the vicinity of laumontite-filled veins. Consequently, both microstructures are spatially linked and are interpreted to have formed simultaneously at a geological time scale. The alignments of tiny fluid inclusions are associated with a small (<0.3°) lattice misorientation visible on the EBSD map in Figure 10b indicating that they result from a combination of brittle and plastic deformation of the quartz lattice. By comparison with experimental studies where fluid inclusion-rich quartz are submitted to a 10^{-8} to 5.10^{-9} strain-rate under 200-600 MPa at 200- 800°C in a Griggs apparatus (Pêcher, 1981; Tarantola et al., 2010) and with similar natural fluid inclusions (Diamond and Tarantola, 2015), alignments of tiny fluid inclusions are tentatively interpreted as decrepitated large former fluid inclusions in an anisotropic stress regime. Decrepitation or dispersion of the former large fluid inclusions was probably accompanied by contamination of the primary fluid by the laumontite-bearing fluid circulating in microfractures and characterizing the first period of seismic activity of the Nojima fault. Decrepitation was then followed by a stress-driven dissolution-diffusion-precipitation mechanism leading to fracture healing and formation of neonate fluid inclusions. It is believed that decrepitation of large fluid inclusions and microfracturing occurred during the seismic stage, and that healing of alignments of tiny fluid inclusions took place during the post-seismic stage. If healing is a slow mechanism at the experimental time-scale (several days or weeks; Pêcher, 1981; Brantley, 1992 ; Tarantola et al., 2010), it may contribute to the relatively fast post-seismic strengthening and seismic velocity recovery observed along active faults during a few months after an earthquake (Brenguier et al., 2008).

In their experiments, Tarantola et al. (2010) have demonstrated that alignments of tiny fluid inclusions form in a plane perpendicular to the maximum compressive stress. Actually, the direction of the alignments of tiny fluid inclusions in the NOJ220 sample is roughly parallel to kink-bands in biotite (Figure S1), which themselves form also perpendicular to the maximum compressive stress (Cummings, 1965). As they are also parallel to the Nojima fault (N50°), this suggests that maximum compressive stress was at high angle to the Nojima fault in the crust when the alignments of tiny fluid inclusions formed. This configuration of stress is consistent with that measured by Ikeda et al. (2001) 1.5 years only after the Kobe earthquake and characterized by the maximum stress being perpendicular to the Nojima fault trace as near the San Andreas fault at Cajon Pass, California (Shamir and Zoback, 1992).

7.3 Plastic deformation of quartz

The maps of crystallographic orientation of quartz in the NOJ220 sample show Dauphiné twins and misorientation domains or subgrains that are indicative of a plastic deformation. The cross-cutting relationships between subgrain boundaries indicate that the large subgrains formed before the small ones and may be attributed to the cooling history of the granodiorite as frequently observed in granitic rocks (Nédélec and Bouchez, 2011). Alteratively as sub-grain size is related to stress during plastic deformation (Sherby et al., 1977) by $\lambda=Ab(\sigma/E)^{-1}$, where A is approximately 4 for many materials, b is the Burgers vector length, σ is stress, and E is Young's modulus, a regime of increasing stress would result in reducing sub-grain sizes nested in larger sub-grains during plastic deformation The small subgrains are elongated parallel to the microfractures and alignments of tiny fluid inclusions suggesting that the three types of microstructures are issued from the same deformation event. If small subgrains or short wave-length misorientations are classically described in rocks deformed at low temperature (see for example Derez et al., 2015) or at high stress and strain-rates (Trepmann, 2009; Trepmann and Stöckert, 2013; Trepmann et al., 2017), as far as we know, association these microstructures with alignments of tiny fluid inclusions has not been described in the literature for a comparison with the NOJ220 sample. Misorientation axes have been determined for quartz in the two areas mapped using EBSD and were identified as [0001] (Figures 5 and 8) or close to [01-11] or [01-12] in the small area mapped with a high resolution (Figure 10). They could give information on the active glide systems provided that their orientation and nature (tilt or twist boundary) are known (Lloyd, 2004). Unfortunately, we did not perform TEM observations to determine dislocation microstructures in the NOJ220 sample. However, more important than the activated glide systems are the small size of the elongated subgrains, the absence of bulging at grain boundaries, and the presence of microfractures that are all together characteristic of a deformation occurring in the semi-brittle faulting regime of quartz as defined by Hirth and Tullis (1994) and Tullis (2002) on the basis of experiments at high strain-rate and low temperature ($>10^{-6}$ s^{-1}, <700°C). The presence of laumontite as a sealing mineral of microfractures indicates a temperature in the range for this regime (<300°C) and, by extrapolation of experimental results to natural conditions, a strain-rate higher than 10^{-5} s^{-1} (Tullis, 2002)., The absence of recrystallization and the small angle of misorientation (<5°) indicate a low finite strain, less than 5% as shown by the maximum shortening measured with (001) cleavages in biotites.

Because of the emergence of new techniques to measure complete crystallographic orientation of quartz, Dauphiné twinning is now recognized in naturally deformed quartz-bearing rocks. Dauphiné twins may form in nature in a wide range of strain-rate conditions from mylonitic quartzites (Lloyd, 2000, 2004 ; Pehl and Wenk, 2005 ; Menegon et al., 2011) to meteoritic impact (Wenk et al., 2005, 2011). Experimental studies were performed to investigate the influence of stress and temperature on Dauphiné twinning and have shown that it initiates at 50-100 MPa at 500°C and that activation twinning is temperature dependent (Wenk et al., 2006). Recently, Wenk et al. (2011) have described Dauphiné twins in quartz from shock experiments, impact structures, pseudotachylites and fault breccias, and conclude that these microstructures are diagnostic of high and transient seismic stresses. Thus, Dauphiné twins observed in quartz from the NOJ220 sample are tentatively attributed to one or possibly several episodes of high and transient seismic stresses. Twinning immediately preceded microfracturing and fragmentation as shown by cross-cuting relationships and their continuity in neighbouring fragments in Figures 5, 8, 9 and 10. Therefore, they are suggested to have formed during the rising stress time before the seismic rupture (Figure 14).

7.4 Elastic strain and residual stress

Elastic strain in a quartz grain was measured with X-ray Laue microdiffraction, which allowed the calculation of the associated residual stress. What could be the origin of the residual stresses measured in quartz? How such large residual stresses may be preserved in such a small volume for such a long time? The fact that residual stresses are measured in a small volume of the thin section suggests that confinement at depth is not the cause of their persistence during long periods of time otherwise they should be released by thin section processing and we should not be able to measure them. As discussed above, the studied quartz display torsions and flexions of the quartz lattice, and subgrains or dislocation walls, which are attributed to dislocation creep under low temperature and high transient stress or strain-rate as quoted above. It is known that a local stress field is associated to each dislocation or dislocation wall because they correspond to a local elastic distorsion of the crystallographic framework (Dieter, 1976 ; Nicolas and Poirier, 1976). Thus, we tentatively interpret the measured residual stresses as the sum of the local stresses attached to each dislocation or dislocation wall present in the quartz grain.

The maps of elastic strain indicate that the ε_{ZZ} component is slightly lower than the others. This could be interpreted as partially released elastic strain close to the free surface of the sample as suggested by Chen et al. (2015), who obtain the same results for a deformed quartz grain in the San Andreas fault zone. However, as the studied NOJ220 thin section is horizontal, such lower ε_{ZZ} component strain component could be also related to the strike-slip tectonic environment of the Nojima fault during the Paleocene (Famin et al., 2014) corresponding to a vertical minimum compressive stress at that geological time. Supplementary X-ray microdiffraction studies on differently orientated thin sections are necessary to test these different interpretations.

The large gradients in elastic strain (xx, yy and zz, yz, xz and xy, Figure S6) are roughly matching the microstructures (subgrain boundaries or microfractures), and they correspond well to the threshold values of the two quality estimators and to the minimum values of diffracted intensity (see Appendix A, Figure A1). Thus, high elastic strain or distorsion of the lattice may prevent a good fitting of the spot positions in the Laue pattern (the single-unit-cell model used to describe the pattern starts to fail). Nevertheless, after filtering these points out, the mean value of residual stress remains high (141 MPa versus 223 MPa if not filtered) in the small 250 x 220 μm^2 studied area included in a single quartz grain (Figures 13b).

We have only performed one scan in the NOJ220 sample using X ray microdiffraction and the representativity of this scan may be questionned. All quartz grains present in the NOJ220 sample display microstructures similar in style and intensity (microfracturing, dispersed fluid inclusions, short wave length misorientation, …) except along the array of very dense microfractures (Figure 6 and 7). Therefore, we think it is possible that the residual stresses measured in such a small studied domain are representative of the whole sample and may represent a lower bound compared to the microfracture array quoted above.

Chen et al. (2015) obtained 130 MPa as a peak in the histogram of residual stresses in a cataclastic quartz sample located 50 m away from the San Andreas Fault active zone in the SAFOD drillhole (California), and 200 MPa in a quartz located within the Vredefort meteoritic impact site in South Africa. Lower values (*ca* 50 MPa) are obtained by Kunz et al. (2009) in the mylonitic (*i.e.* plastically deformed) Santa Rosa granite (California). Thus, our results (peak at 100 MPa, mean at 141 MPa) compare well to the values published by Chen et al. (2015) for quartz samples of the San Andreas fault zone although the NOJ220 studied sample is located outside of the damage zone of the Nojima fault.

As pointed out by Chen et al. (2015) the residual stresses have remained in the crystals for very long time, as long as 2 b.y. in the case of the Vredefort impact. In the Nojima fault sample, elastic strain and residual stress have been preserved since 56 Ma, age of the first period of seismic activity of the fault (Murakami and Tagami, 2004) and were not released during the uplift of the area from 3.7-11.1 km depth (depth range of laumontite stability) to the near surface (<1 km depth), or during the Quaternary phase of seismic activity of the Nojima fault since 1.2 Ma. We believe that internal stresses could not be released after dynamic damage due to the very low temperature (<300°C) inhibiting reorganization of dislocations and recrystallization of quartz, the later being a potential marker of stress relaxation (Trepmann et al., 2017).

7.5 Implications for the development of the damage zone

As discussed above, we interpret the laumontite-filled veins, the microfractures and fluid inclusion decrepitation as resulting from a co-seismic fracturation and the Dauphiné twinning and plastic deformation of quartz as a high strain-rate precursor of the same dynamic event that left behind high residual stresses in the sample (peak at 100 MPa, mean at 141 MPa). Earthquakes characterizing the first period of seismic activity along the Nojima fault were M6 to M7 magnitude events (Boullier et al., 2001) and their consequences may be compared to those of californian earthquakes along the San Andreas fault system where pulverized rocks were produced on the near surface within a 100 m wide zone (Dor et al., 2006 ; Rockwell et al., 2009). We believe that microstructures in the NOJ220 sample are representative of the incipient dynamic damage at depth induced by the propagation of a seismic rupture on the Nojima fault plane 51 m away from the studied sample. Imprints of this damage are resumed to a few fractures which are now sealed within laumontite, and to residual stress and microscale deformation structures in quartz. We postulate that successive seismic ruptures would cumulate residual stresses until exceeding the strength of the rock. While the strength of the undeformed and unaltered protolith of the Nojima fault is around 400 MPa at an effective confining pressure of 50 MPa, samples located at 14.5 m and 5 m from the fault plane have a 200 MPa and 150 MPa strength, respectively (Lockner et al., 2009). Thus, the residual stresses accumulated in the studied NOJ220 sample are close to that of the damaged granodiorite and could have contributed to the enlargment of the observed 45m wide damage zone (Ohtani et al., 2000a ; Tanaka et al., 2001).

As pointed already, microstructures in the NOJ220 sample are very similar to the experimentally or naturally fragmented samples described by Aben et al. (2016) and Dor et al. (2006, 2009) and Rockwell et al. (2009) repectively. We know that high confining pressure prevents complete pulverization but not fragmentation (Yuan et al., 2011). The confining pressure being in the 100 - 300 MPa range when microstructures formed in the NOJ220 sample, the strain-rate threshold was probably not attained and the granodiorite was microfractured, but not pulverized. The high stresses associated with the propagating seismic waves have induced elastic strain, which has not been completely released by the microfracturing process, and which could be measured today by X-ray microdiffraction.

In their experiments, Aben et al. (2016) have shown that the pulverization threshold can be reduced by successive dynamic loadings at lower strain-rate if the rock experiences dynamic fracturing during successive loadings. They show that each dynamic event leads to the growth of additional microfractures homogeneously distributed and that P-wave velocity decreases with an increasing amount of damage. P and S-wave velocities have been measured on the GSJ Hirabayashi drillcore samples by Zamora et al. (2000). At 204m depth (d_{fault} = 53.2 m) mean V_P is 5320 $m.s^{-1}$ on dry samples but falls at 4950 $m.s^{-1}$ at 220m depth (d_{fault} = 51.3 m) in the same core piece as the sample studied in this paper. Such a 7% decrease in V_P velocity is another indicator for dynamic damage in the sample. An important difference between experiments and natural fault zones is that fluid circulates during the interseismic period. Post-seismic hydrothermal healing of the dynamically created microfractures partially increase the strength of rocks as laumontite does in the Nojima samples (Figure 14). Nevertheless, high stresses measured today by X-ray microdiffraction may be considered as a recording of the propagating seismic waves along the Nojima fault.

8 Conclusions

We have studied a core sample of granodiorite located at 51.3 m from the Nojima fault (Japan) that was drilled after the Hyogo-ken Nanbu (Kobe) earthquake using EBSD and high resolution X-ray Laue microdiffraction. Although macroscopically undeformed, the sample is pervasively microfractured and locally fragmented during the first stage of seismic activity along the Nojima fault. On the basis of the sealing hydrothermal laumontite, we are able to estimate that microfracturing occurred at 100-300 MPa confining pressure, *i.e.* at 3.7 – 11.1 km depth. EBSD mapping was used to characterize the crystallographic orientations and deformation microstructures in the sample, and X-ray Laue microdiffraction to measure elastic strain and residual stresses in a quartz grain. Both methods give consistent results on the crystallographic orientation and show small and short wave-length misorientations associated with laumontite-sealed microfractures and alignments of tiny fluid inclusions. Deformation microstructures are symptomatic of the semi-brittle faulting regime in which low temperature brittle and plastic deformation and stress-driven dissolution-deposition processes occur conjointly.

Using the Hooke's law, residual stresses are calculated from elastic strain measured by X-ray microdiffraction and peaks at 100 MPa (mean 141 MPa), a value similar to that obtained on quartz located at 50 m from to the San Andreas fault gouge. Such stress values are comparable to the peak strength of a damaged granodiorite from the damage zone around the Nojima fault indicating that, although apparently macroscopically undeformed, the sample is actually significantly damaged. The homogeneously distributed microfracturing of quartz is the microscopically visible imprint of this damage and suggests that high stresses were stored in the whole sample and not only concentrated on some crystal defects. It is proposed that the high residual stresses are the sum of the stress fields associated with dislocations and dislocation microstructures that were triggered by the dynamic damage related to the propagation of rupture fronts or seismic waves associated to M6 to M7 earthquakes during Paleocene on the Nojima fault at a 3.7 – 11.1 km depth where the *in situ* confining pressure prevented pulverization. The high residual stresses and the deformation microstructures would have contributed to the enlargment or widening of the fault zone with additional large earthquakes occurring on the Nojima fault.

9 Appendix A - X-ray Laue microdiffraction : method and parameters for the analysis of the series of Laue patterns

The methods for sample alignment and geometry calibration using the Laue pattern of a Ge single crystal were described in Ulrich et al. (2011). The three main stages of automated analysis of a Laue pattern (peak search, indexation, unit cell dimensions and orientation refinement) were described in Tamura (2014) and Robach (2017), and also in the documentation of the LaueTools software.

For the quartz sample studied here, as described in figure 2c, two types of Laue patterns are encountered : type 1 : single-crystal (one spot per HKL) Laue patterns, (about 70% of the map) and type M : multiple closely-oriented subgrains (several sub-spots per HKL) Laue patterns (about 30% of the map). For type 1 points, the orientation and strain results are essentially "single-valued", *i.e.* are reproducible over a wide range of analysis parameters.

For type M points, a criterion needs to be arbitrarily chosen in order to decide which is "the" x,y position of a multi-spot or an asymmetrical spot. Indeed, although in theory a multi-grain indexation procedure could be applied to the multi-spot Laue pattern, in order to individually index each sub-spot present on the beam path, in practice the corresponding code for closely-spaced sub-spots is still unavailable. And at the stage of the display of the 2D maps of strain or orientation, a decision needs to be taken in any case, in order to select the individual sub-grain or the mean grain to be displayed at each point. For type M points, results therefore widely vary depending on analysis parameters such as i) the box size for the 2D Gaussian fitting of the spots in the Peak Search stage, ii) the angular tolerance for linking theoretical (undeformed reference crystal) and experimental spots at the SpotLink stage of the Indexation stage, and iii) the threshold on pixel deviation for removing bad spots at the refinement stage.

In addition, there is a limit to the "indexability" of M points : when the groups of sub-spots are too wide, neighbouring groups of sub-spots belonging to different HKL's start to intersect, and the number of indexed spots falls. For a type 1 point, the typical minimum distance between experimental spots is 17 pixels. This sets an upper limit on the width (in pixels) of the groups of sub-spots, above which the brute-force spot-linking process based on pixel-distance only starts to produce ambiguous results (e.g. double-indexed experimental spots or double-linked theoretical spots).

An arbitrary choice was therefore needed for the analysis of the M points. Different indexation strategies were envisaged: a first approach is to try to select the sub-grain closest to the surface, either by selecting the most intense sub-spot in each group (based on maximum pixel intensity, or maximum integrated intensity), or by spot-linking directly on the local orientation matrix determined with EBSD, taking advantage of the near surface-sensitivity of EBSD. Assuming that the angular accuracy of classical EBSD is around 0.3 degrees (5.2 mrad), the EBSD-approach would only work if the sub-spots in each group were distant by more than 5 pixels. A second approach, the one choosen in this paper, is to average over all the sub-spots of the M point to create an "average sub-grain".

9.1 « One-spot » analysis

Figure A1 illustrates the variations in the orientation maps produced by a change in the criterion used to calculate the x,y position of the experimental multi-spot (M point). Here a box of 201x201 pixels around the position x_pix,y_pix = (1484,1213) ((02-22) spot of Figure 2b) was extracted from the patterns. The positions xy_max and xy_fit of the spot were calculated by taking, for xy_max, the (integer) pixel position of the maximum of intensity, and for xy_fit, the (real) center position of the 1D Gaussian obtained by fitting the intensity profile projected onto the y axis (respectively the x axis) for the x position (respectively the y position). The positions xy_max and xy_fit are mapped in Figure A1a and A1b respectively. This very simple "one-spot" analysis already allows visualizing the sub-grain structure inside the mapped region. Indeed, as a first approximation, the x (respectively y) position of the spot provides the crystal orientation in rotation around the y axis (Ry) (respectively Rx).

For M points, the choice of xy_max approximately selects the sub-grain closest to the surface, assuming that its crystalline quality remains sufficient to always dominate with respect to deeper sub-grains. The choice of xy_fit corresponds to building an "average grain" at each map point, with a diffraction-wise averaging, *i.e.* giving a larger weight to well-crystallized region, performed over the different sub-grains present on the beam path.

The most remarkable difference between the (a) and (b) maps in Figure A1 is the sharper aspect of the sub-grain edges in (a). The averaging over depth in (b) therefore leads, as expected, to a degraded lateral resolution, especially when crossing non-vertical sub-grain boundaries (with respect to the thin section). When comparing the sub-grain structure between Figure A1 and the EBSD misorientation maps of Figure 11b, a closer similarity with (a) is observed, as expected for a criterion attempting to select the sub-grain closest to the surface at each point.

9.2 « N-spots » analysis

For the N-spots analysis of the Laue patterns, the xy_fit criterion was used (average sub-grain for type M points). The sub-grain edges in the final micro-Laue strain and orientation maps are therefore less sharp than in the EBSD maps.

Since the region mapped with X-rays was inside in a single grain, the analysis of the series of Laue patterns was performed using a "light-weight" two-spots method to obtain the first "guess orientation matrix". Indeed, the "brute force" indexation of a quartz pattern is a CPU-consuming process due to the low symmetry of the crystal and the corresponding large number of possible theoretical angular distances between crystal planes, and a lighter procedure is preferable when processing a large number of images. Here classical indexation was applied to only one pattern, then two widely-spaced low-Miller-index spots were selected : the (02-22) spot (spot 2) already analyzed in Figure 14, and the (-2203) spot (spot 1) located around xypix = (659,1640). The interest of using low-index spots is that their first neighbor is comparatively far away (147 pixels for spot 2 and 131 pixels for spot 1) : the risk of a spot with a different (HKL) entering the fixed 201x201 pixels-wide box, due to the rotation of the crystal, is therefore limited. In practice, the highest spot displacement with respect to the box center (using xy_fit) was 147 pixels for spot 2 and 57 pixels for spot 1. After excluding 11 "bad" points (over a total of 9077) the highest displacement for spot 2 was down to 58 pixels.

The two-spot analysis of the series of Laue patterns was performed using the xy_fit positions for the spots. The resulting approximate orientation matrix (with an unstrained unit cell) was then used to perform a spot-link (linking each theoretical spot to its nearest experimental neigbor) with the list of spots resulting from the peak-search procedure. The angular tolerance (between reciprocal lattice vectors) for the spot-linking process was 0.2 degrees.

Three estimators (npeaks, pixdev, and intensity) of the local uncertainty on the shape / orientation of the unit cell, were calculated with the LaueTools software (Figure A2). The first estimator (npeaks) is the number of Laue spots used for the refinement of the local orientation and the distorted quartz unit cell. For map points with single sharp spots, a low npeaks gives good data quality (npeaks > 15, Figure A2a). For map points with multiple spots (several subgrains in the beam path), a high npeaks is needed for good data quality (npeaks > 25, Figure A2), since the position of each "average" HKL spot is less accurate. The second estimator (pixdev, mean pixel deviation, Figure A2b) is a measure of the fit quality and represents the mean distance between the experimental (as estimated from 2D peak fitting on the detector image) and theoretical (as calculated from the refined orientation and distorted unit cell) x,y pixel positions of the Laue spots, averaged over the npeaks spots of the pattern. One pixel of pixdev typically gives an uncertainty of 10^{-3} mrad^{-1} on the strain / orientation components. The third estimtor is the intensity and represents the average intensity of the 10 most intense spots of the Laue pattern of the grain (Figure A2c). The spot intensity is the height (peak minus background) of the 2D Gaussian used to fit the 2D image in a box of 101 x 101 pixels around the spot center (boxsize = 50). The search for local maxima in the image (which produces the list of x,y pixel positions of spot centers) was performed using the "convolution" method, which proceeds as follows : first the image is convoluted with a 2D mexican hat function with a FWHM of 3 pixels. This attributes all the Laue spots with a similar width. Thresholding is then applied on the convoluted image (thresholdConvolve = 3000), producing a first mask. The intense pixels in this mask are then grouped by clusters (blobs) based on a "+"-like connectivity criterion. The list of clusters is then reduced by applying a criterion of a minimal distance between two clusters (PixelNearRadius = 50 pixels). The list of remaining clusters is then reduced again by thresholding on the non-convoluted image, after subtracting the local background : Iraw - Ibackground > 50 (IntensityThreshold = 50) where Ibackground is the mean intensity on the frame of a box of 101x101 pixels (boxsize = 50) centered on the cluster center. The resulting mask is shown on Figure A2d.

After the spot-link stage, the orientation and shape of the unit cell (strained orientation matrix) was refined once using the N indexed spots, then the new pixel deviation (pixdev) between experimental and theoretical spots was calculated, and the refinement was run again after excluding spots with a pixdev larger than 3. This leads to the final values for npeaks and pixdev displayed in Figure A2a and Figure A1b. Figure A2 illustrates the filtering used for the final display of the elastic strain maps of Figures 12 and S5.

Finally, we remark that more complete maps (in terms of number of points) can be obtained using only the two-spots analysis. Figure A3 shows the lattice rotation and strain results in this analysis, performed using xy_max instead of xy_fit. Only one scalar strain component is available is this analysis. The strain results obtained using xy_fit are also shown.

Author contribution:

AMB performed the microstructural study and participated to EBSD acquisition. OR performed the X-ray Laue microdiffraction data acquisition and processing. FB acquired the EBSD data. BI and DM processed the EBSD data using MTEX. TO and KF provided the sample and the geological knowledge of the GSJ borehole. All co-authors participated to the interpretation and discussion of results. AMB prepared the manuscript with contributions from all co-authors.

Competing interests:

The authors declare that they have no conflict of interest.

Acknowledgements

The authors thanks M. Bouchon, J. Weiss, M. Montagnat and M.-L. Doan who have greatly contributed to improve a first version of this paper and particularly by discussing the seismological and mechanical implications of our results. Friendly and fruitfull discussions with D. Amitrano and F. Aben on quasi-static and dynamic damage are sincerely acknowledged. The authors thank Olivier Ulrich for assistance with the micro-Laue setup and Jean-Sébastien Micha for help using the LaueTools software. Christophe Nevado is thanked for high quality thin section polishing and Valentina Batanova and Valérie Magnin for their help using SEM cathodoluminescence.

References

Aben, F. M., Doan, M.-L., Mitchell, T. M., Toussaint, R., Reuschlé, T., Fondriest, M., Gratier, J.-P., and Renard, F.: Dynamic fracturing by successive coseismic loadings leads to pulverization in active fault zones., J. Geophys. Res.- Sol. Ea., 121, 2338–2360, 10.1002/2015JB012542, 2016.

Austrheim, H., Dunkel, K., Plümper, O., Ildefonse, B., Liu, Y., and Jamtveit, B.: Fragmentation of wall rock garnets during deep crustal earthquakes., Science Advances, 3, e1602067, 2017.

Bachmann, F., Hielscher, R., and Schaeben, H.: Texture analysis with MTEX–free and open source software toolbox., Solid State Phenom. 160, 63-68, 10.4028/www.scientific.net/SSP.160.63, 2010.

Blenkinsop, T. G., and Sibson, R. H.: Aseismic fracturing and cataclasis involving reaction softening within core marerial from the Cajon Pass drill hole, J. Geophys. Res., 97, 5135-5144, 1992.

Bouchon, M.: The state of stress on some faults of the San Andreas system as inferred from near-field strong motion data, J. Geophys. Res., 102, 11731-11744, 1997.

Boullier, A.-M.: Fault zone geology : lessons from drillings through Nojima and Chelungpu faults, in: Geology of the Earthquake Source : A Volume in Honour of Rick Sibson, edited by: Fagereng, A., and Toy, V., Sp. Pub., 359, Geol. Soc. London, 17-37, 2011.

Boullier, A.-M., Fujimoto, K., Ito, H., Ohtani, T., Keulen, N., Fabbri, O., Amitrano, D., Dubois, M., and Pezard, P.: Structural evolution of the Nojima fault (Awaji Island, Japan) revisited from the GSJ drill hole at Hirabayashi, Earth Planets Space, 56 (12), 1233-1240, 2004a.

Boullier, A.-M., Fujimoto, K., Ohtani, T., Roman-Ross, G., Lewin, E., Ito, H., Pezard, P., and Ildefonse, B.: Textural evidence for recent co-seismic circulation of fluids in the Nojima fault zone, Awaji island, Japan, Tectonophysics, 378, 165-181, 2004b.

Boullier, A.-M., Ohtani, T., Fujimoto, K., Ito, H., and Dubois, M.: Fluid inclusions in pseudotachylytes from the Nojima fault, Japan, J. Geophys. Res.- Sol. Ea., 106, 21965-21977, 2001.

Brantley, S. L.: The effect of fluid chemistry on quartz microcrack lifetimes, Earth Planetary Sc. Lett., 113, 145-156, 1992.

Brenguier, F., Campillo, M., Hadziioannou, C., Shapiro, N. M., Nadeau, R. M., and Larose, E.: Postseismic relaxation along the San Andreas fault at Parkfield from continuous seismological observations, Science, 321, 1478-1481, 10.1126/science.1160943, 2008.

Chen, K., Kunz, M., Tamura, N., and Wenk, H.-R.: Residual stress preserved in quartz from the San Andreas Fault Observatory at Depth, Geology, 43, 219-222, 2015.

Chester, F. M., and Chester, J. S.: Ultracataclasite structure and friction processes of the Punchbowl fault, San Andreas system, California, Tectonophysics, 295, 199-221, 1998.

Cho, M., Maruyama, S., and Liou, J. G.: An experimental investigation of heulandite-laumontite equilibrium at 1000 to 2000 bar Pfluid, Contrib. Mineral. Petr., 97, 40-50, 1987.

Cummings, D.: Kink-bands : shock deformation of biotite resulting from a nuclear explosion, Science, 148, 950-952, 1965.

Derez, T., Pennock, G., Drury, M., and Sintubin, M.: Low-temperature intracrystalline deformation microstuctures in quartz, J. Struct. Geol., 71, 3-23, 10.1016/j.jsg.2014.07.015, 2015.

Diamond, L. W., and Tarantola, A.: Interpretation of fluid inclusions in quartz deformed by weak ductile shearing : reconstruction of differential stress magnitudes and pre-deformation fluid properties, Earth Planetary Sc. Lett., 417, 107-119, 2015.

Dieter, G. E.: Mechanical metallurgy, Material Science and Engineering Series, McGraw-Hill, Inc., 774 pp., 1961.

Doan, M. L., and Gary, G.: Rock pulverization at high strain rate near the San Andreas fault, Nat. Geosci., 2, 709-712, 2009.

Dor, O., Ben-Zion, Y., Rockwell, T. K., and Brune, J.: Pulverized rocks in the Mojave section of the San Andreas Fault Zone, Earth Planetary Sc. Lett., 245, 642-654, 2006.

Dor, O., Chester, J. S., Ben-Zion, Y., Brune, J. N., and Rockwell, T. K.: Characterization of damage in sandstones along the Mojave Section of the San Andreas Fault: implications for the shallow extent of damage generation, Pure Appl. Geophys., 166, 1747-1773, 2009.

Fabbri, O., Iwamura, K., Matsunaga, S., Coromina, G., and Kanaori, Y.: Distributed strike-slip faulting, block rotation, and possible intracrustal vertical decoupling in the convergent zone of southwest Japan, in: Vertical Coupling and Decoupling of the Lithosphere, edited by: Grocott, J., Tikoff, B., McCaffrey, K. J. W., and Taylor, G., Sp. Pub., 227, Geol. Soc. London, 141–166, 2004.

Famin, V., Raimbourg, H., Garcia, S., Bellahsen, N., Hamada, Y., Boullier, A.-M., Michon, L., Revil, A., Uchide, T., Ricci, T., Hirono, T., and Kawabata, K.: Stress rotations and the long-term weakness of the Median Tectonic Line and the Rokko-Awaji segment, Tectonics, 33, 1900-1919, 10.1002/2014TC003600, 2014.

Fauré, J.: Recherches sur les effets géologiques d'explosions atomiques souterraines dans un massif de granite saharien, Faculté des Sciences, Université de Nancy, 433 pp., 1970.

Fujimoto, K., Ueda, A., Ohtani, T., Takahashi, M., Ito, H., Tanaka, H., and Boullier, A. M.: Borehole water and hydrologic Nojima fault, SW model around the Japan, Tectonophysics, 443, 174-182, 2007.

Hickman, S., and Zoback, M.: Stress orientations and magnitudes in the SAFOD pilot hole, Geophys. Res. Lett., 31, L15S12, 10.1029/2004GL020043, 2004.

Hielscher, R., and Schaeben, H.: A novel pole figure inversion method: specification of the MTEX algorithm, J.Appl. Crystallogr., 41, 1024-1037, 10.1107/S0021889808030112, 2008.

Hilgers, C., Köhn, D., Bons, P. D., and Urai, J. L.: Development of crystal morphology during unitaxial growth in a progressive widening vein: II. Numerical simulations of the evolution of antitaxial fibrous veins, J. Struct. Geol., 23, 873-885, 2001.

Hirth, G., and Tullis, J.: The brittle-plastic transition in experimentally deformed quartz aggregates, J. Geophys. Res., 99, 11731-11747, 1994.

Ikeda, R., Iio, Y., and Omura, K.: In situ stress measurements in NIED boreholes in and around the fault zone near the 1995 Hyogo-ken Nanbu earthquake, Japan, Isl. Arc, 10, 252-260, 2001.

Ito, H., Kuwahara, Y., Kiguchi, T., Fujimoto, K., and Ohtani, T.: Outline of the Nojima Fault drilling by GSJ : structure, physical properties and permeability structure from borehole measurements in GSJ borehole crossing the Nojima Fault, Japan, Proceedings of the International workshop on the Nojima fault core and borehole analysis, Tsukuba, Japan, 1999, 71-79, 2000.

Kanaori, Y.: Late Mesozoic-Cenozoic strike-slip and block rotation in the inner belt of Southwest Japan, Tectonophysics, 177, 381-399, 1990.

Kunz, M., Chen, K., Tamura, N., and Wenk, H.-R.: Evidence for residual elastic strain in deformed natural quartz, Am. Mineral., 94, 1059-1062, 2009.

Lin, W., Kwasniewski, M., Imamura, T., and Matsuki, K.: Determination of three-dimensional in situ stresses from anelastic strain recovery measurements of cores at great depth, Tectonophysics, 426, 221-238, 2006.

Lloyd, G. E.: Grain boundary contact effects during faulting of quartzite: an SEM/EBSD analysis, J. Struct. Geol., 22, 1675-1693, 2000.

Lloyd, G. E.: Microstructural evolution in a mylonitic quartz simple shear zone : the significant roles of Dauphiné twinning and misorientation, in: Flow processes in faults and shear zones, edited by: Alsop, G. I., Holdswoorth, R. E., McCaffrey, K. J. W., and Hand, M., Sp. Pub., 224, Geol. Soc. London, 39-61, 2004.

Lockner, D. A., Tanaka, H., Ito, H., Ikeda, R., Omura, K., and Naka, H.: Geometry of the Nojima Fault at Nojima-Hirabayashi, Japan - I. A Simple Damage Structure Inferred from Borehole Core Permeability, Pure Appl. Geophys., 166, 1649-1667, 2009.

Mainprice, D., Lloyd, G. E., and Casey, M.: Individual Orientation Measurements in Quartz Polycrystals - Advantages and Limitations for Texture and Petrophysical Property Determinations, J. Struct. Geol., 15, 1169-1187, 1993.

Menegon, L., Piazolo, S., and Pennacchioni, G.: The effect of Dauphiné twinning on plastic strain in quartz, Contrib. Mineral. Petr, 161, 635-652, 2011.

Mainprice, D., Bachmann, F., Hielscher, R., and Schaeben, H.: Descriptive tools for the analysis of texture projects with large datasets using MTEX: strength, symmetry and components, in: Rock Deformation from Field, Experiments and Theory: A Volume in Honour of Ernie Rutter, edited by: Faulkner, D. R., Mariani, E., and Mecklenburgh, J., Sp. Pub., 409, Geol. Soc. London, 251-271, 2014.

Mitchell, T. M., Ben-Zion, Y., and Shimamoto, T.: Pulverized fault rocks and damage asymmetry along the Arima-Takatsuki Tectonic Line, Japan, Earth Planetary Sc. Lett., 308, 284-297, 10.1016/j.epsl.2011.04.023, 2011.

Murakami, M., and Tagami, T.: Dating pseudotachylyte of the Nojima fault using the zircon fission-track method, Geophys. Res. Lett., 31, L12604, 10.1029/2004GL020211, 2004.

Nédélec, A., and Bouchez, J.-L.: Pétrologie des granites : structure, cadre géologique, Interactions, edited by: De Wever, P., Société Géologique de France, Vuibert, Paris, 306 pp., 2011.

Nicolas, A., and Poirier, J.-P.: Crystalline plasticity and solid-state flow in metamorphic rocks, J. Wiley Interscience Publications, London, 444 pp., 1976.

Ogi, H., Ohmori, T., Nakamura, N., and Hirao, M.: Elastic, anelastic, and piezoelectric coefficients of α-quartz determined by resonnance ultrasound spectroscopy, J. Appl. Phys., 100, 053511, 2006.

Ohtani, T., Fujimoto, K., Ito, H., Tanaka, H., Tomida, N., and Higuchi, T.: Fault rocks and past to recent fluid characteristics from the borehole survey of the Nojima fault ruptured in the 1995 Kobe earthquake, southwest Japan, J. Geophys. Res., 105, B7, 16161-16171, 2000a.

Ohtani, T., Miyazaki, T., Tanaka, H., Kiguchi, T., Fujimoto, K., and Ito, H.: Reorientation of cores and distribution of macroscopic fractures along the GSJ borehole penetrating the Nojima fault zone, International workshop of the Nojima fault core and borehole data analysis, Tsukuba, Japan, 1999, 271-276, 2000b.

Pêcher, A.: Experimental decrepitation and reequilibration of fluid inclusions in synthetic quartz, Tectonophysics 78, 567-584, 1981.

Pehl, J., and Wenk, H.-R.: Evidence for regional Dauphiné twinning in quartz from the Santa Rosa mylonite zone in Southern California. A neutron diffraction study, J. Struct. Geol., 27, 1741–1749, 2005.

Petit, J., Castelnau, O., Bornert, M., Zhang, F. G., Hofmann, F., Korsunsky, A. M., Faurie, D., Le Bourlot, C., Micha, J. S., Robach, O., and Ulrich, O.: Laue-DIC: a new method for improved stress field measurements at the micrometer scale, J. Synchrotron Radiat., 22, 980–994, 10.1107/S1600577515005780, 2015.

Reches, Z., and Dewers, T. A.: Gouge formation by dynamic pulverization during earthquake rupture, Earth Planetary Sc. Lett., 235, 361-374, 10.1016/j.epsl.2005.04.009, 2005.

Robach, O., Micha, J.-S., Ulrich, O., Devincre, B., Hoc, T., Daveau, G., Consonni, V., and Petit, J.: Analyse avancée des contraintes et des gradients d'orientation par microdiffraction Laue des rayons X, in: Rayons X et Matière, edited by: Goudeau, P., and Guinebretière, R., 2017, to be published.

Rockwell, T., Sisk, M., Girty, G., Dor, O., Wechsler, N., and Ben-Zion, Y.: Chemical and Physical Characteristics of Pulverized Tejon Lookout Granite Adjacent to the San Andreas and Garlock Faults: Implications for Earthquake Physics, Pure Appl. Geophys., 166, 1725-1746, 2009.

Roedder, E.: Fluid inclusions, Reviews in Mineralogy, 12, Mineralogical Society of America, 644 pp., 1984.

Sagy, A., and Korngreen, D.: Dynamic branched fractures in pulverized rocks from a deep borehole, Geology, 40, 799-802, 2012.

Shamir, G., and Zoback, M. D.: Stress orientation profile to 3.5 km depth near the San Andreas Fault at Cajon Pass, California, J. Geophys. Res., 97, 5059-5080, 1992.

Sibson, R. H.: Fault rocks and fault mechanisms, J. Geol. Soc. London, 191-213, 1977.

Sibson, R. H.: Thickness of the seismic slip zone, B. Seismol.l Soc. Am., 93, 1169-1178, 2003.

Sherby, O. D., Klundt, H. R., and Miller, A. K.: Flow stress, subgrain size, and subgrain stability at elevated temperature, Metall. Trans. A, 8, 843-850, 1977.

Tamura, N.: XMAS : a versatile tool for analyzing synchrotron X-ray microdiffraction data, in: Strain and dislocation gradients from diffraction, edited by: Barabash, R. I., and Ice, G. E., Imperial College Press / World Scientific Publishing, 125-155, 2014.

Tanaka, H., Fujimoto, K., Ohtani, T., and Ito, H.: Structural and chemical characterization of shear zones in the freshly activated Nojima fault, Awaji Island, southwest Japan, J. Geophys. Res., 106, 8789–8810, 2001.

Tarantola, A., Diamond, L. W., and Stunitz, H.: Modification of fluid inclusions in quartz by deviatoric stress I: experimentally induced changes in inclusion shapes and microstructures, Contrib. Mineral. Petr, 160, 825-843, 2010.

Trepmann, C. A.: Shock effects and pre-shock microstructures in hydrothermal quartz veins from the Rochechouart impact structure, France, J. Struct. Geol., 31, 1183-1196, 0.1016/j.jsg.2009.06.017, 2009.

Trepmann, C. A., and Stöckert, B.: Cataclastic deformation of garnet : a record of synseismic loading and postseismic creep, J. Struct. Geol., 24, 1845-1856, 2002.

Trepmann, C. A., and Stöckert, B.: Short-wavelength undulatory extinction in quartz recording coseismic deformation in the middle crust – an experimental study, Solid Earth, 4, 263-276, 10.5194/se-4-263-2013, 2013.

Trepmann, C. A., Hsu, C., Hentschel, F., Döhler, K., Schneider, C., and Wichmann, V.: Recrystallization of quartz after low-temperature plasticity - The record of stress relaxation below the seismogenic zone, J. Struct. Geol., 95, 72-92, 10.1016/j.jsg.2016.12.004, 2017.

Tullis, J.: Deformation of granitic rocks : experimental studies and natural examples, in: Plastic deformation of minerals and rocks, edited by: Karato, S.-I., and Wenk, H.-R., Rev. Mineral. Geochem., 51, Mineral. Soc. Am., Geochem. Soc., 51-95, 2002.

Ulrich, O., Biquard, X., Bleuet, P., Geaymond, O., Gergaud, P., Micha, J. S., Robach, O., and Rieutord, F.: A new white beam X-ray microdiffraction setup on the BM32 beamline at the European Synchrotron Radiation Facility, Rev. Sci. Instrum., 82, 033908, 2011.

Wechsler, N., Allen, E. E., Rockwell, T. K., Girty, G., Chester, J. S., and Ben-Zion, Y.: Characterization of pulverized granitoids in a shallow core along the San Andreas Fault, Littlerock, CA, Geophys. J. Int., 186, 401-417, 0.1111/j.1365-246X.2011.05059.x, 2011.

Wenk, H.-R., Janssen, C., Kenkmann, T., and Dresen, G.: Mechanical twinning in quartz : shock experiments, impact, pseudotachylites and fault breccias, Tectonophysics, 510, 69-79, 2011.

Wenk, H.-R., Lonardelli, I., Vogel, S. C., and Tullis, J.: Dauphiné twinning as evidence for an impact origin of preferred orientation in quartzite ; an example from Vredefort, South Africa, Geology, 33, 273-276., 2005.

Wenk, H.-R., Rybacki, E., Dresen, G., Lonardelli, I., Barton, N., Franz, H., and Gonzalez, G.: Dauphiné twinning and texture memory in polycrystalline quartz. Part 1: Experimental deformation of novaculite, Phys.Chem. Miner., 33, 667-676, 2006.

Xia, K., Nasseri, M. H. B., Mohanty, B., Lu, F., Chen, R., and Luo, S. N.: Effects of microstructures on dynamic compression of Barre granite, Int. J. Rock Mech. Min., 45, 879-887, 2008.

Yuan, F., Prakash, V., and Tullis, T.: Origin of pulverized rocks during earthquake fault rupture, J. Geophys. Res.- Sol. Ea., 16, B06309, 10.1029/2010JB007721, 2011.

Zamora, M., Pézard, P. A., and Ito, H.: Anisotropy of elastic and anelastic properties of granites from the Hirabayashi hole, Japan, International workshop of the Nojima fault core and borehole data analysis, Tsukuba, Japan, 1999, 227-231, 2000.

Zoback, M. D., and Healy, J. H.: In situ measurements to 3.5 km depth in the Cajon Pass scientific research borehole: implications for the mechanics of crustal faulting, J. Geophys. Res., 97, 5039-5057, 1992.

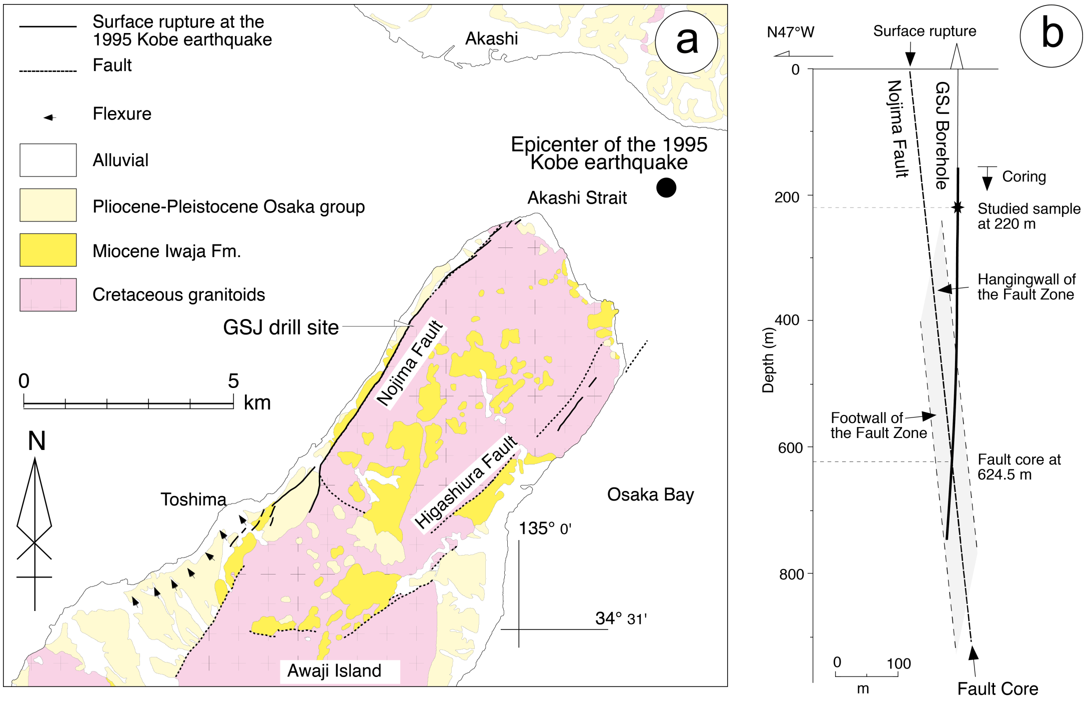

Figure 1 : Geological setting. a) Geological map of the Awaji Island showing the Nojima fault and the location of the GSJ Hirabayashi drillhole (modified from Ohtani et al., 2000a). b) Schematic cross-section showing the relative geometries of the Nojima fault and the GSJ drillhole.

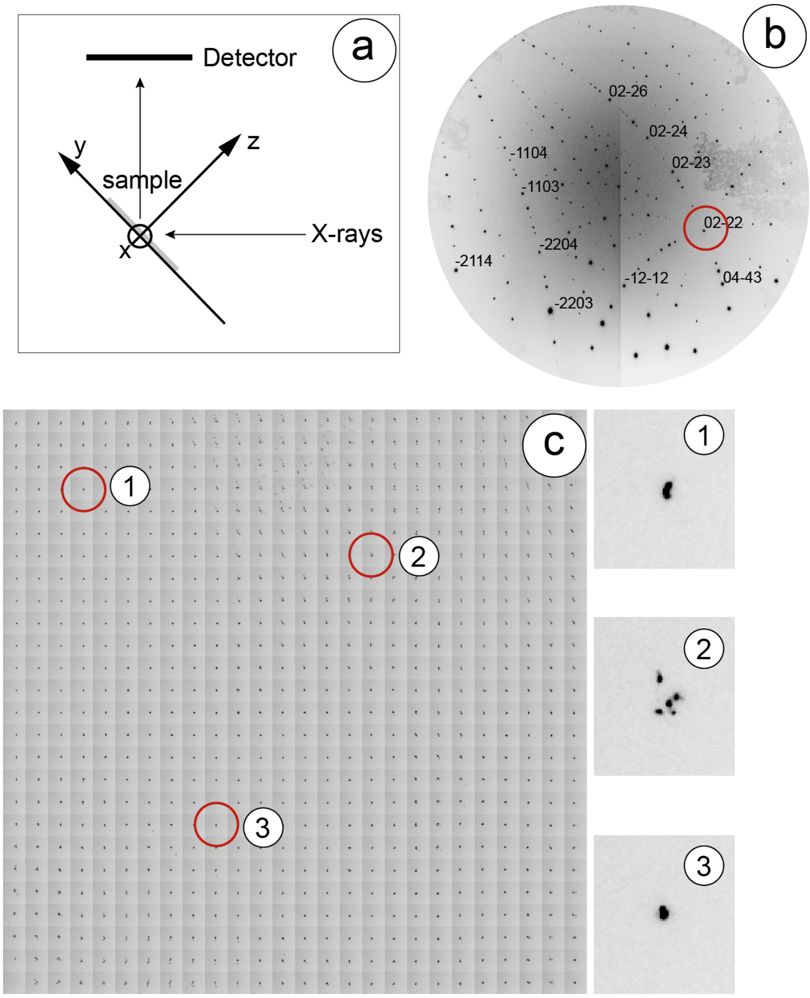

Figure 2 –Laue X-ray microdiffraction. a) Geometric disposition of the sample relative to the X-rays beam and definition of the x, y and z axes of the sample referential. A more detailed definition of the sample reference frame is provided in Petit et al. (2015). b) Laue image corresponding to the point indicated by the red circle 3 on the map ; some spots are indexed, especially the [02-22] spot (red circle) which has been used for the following mosaic map. The detector image is oriented as the one that would be seen by an observer lying at the place of the sample and receiving the incident beam on the top of the head. c) 26 x 26 points mosaic map constructed with a 10 µm step on the quartz grain analyzed in Figure 4. The [02-22] spot location, shape and intensity on the detector vary on each step depending on the orientation, crystallinity and deformation of the crystal. In the point 2 of the map, multiple spots are indicative of several subgrains present in the analyzed volume; in point 1, the [02-22] spot is elongated in a NNW-SSE direction indicating a continuous bending of the crystal lattice roughly around the x axis (Robach, 2017).

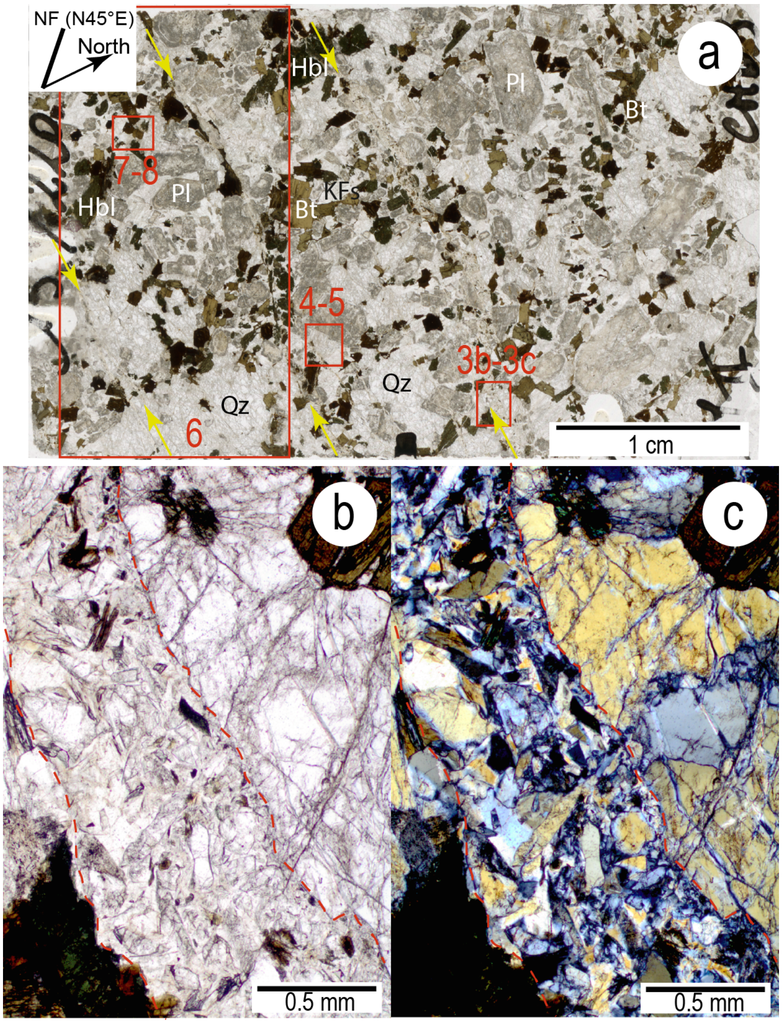

Figure 3 : The NOJ220 thin section (45 x 30 mm). a) Scan showing the overall preserved magmatic texture. The orientation of the thin section is inverse and indicated in the top left box (NF : Nojima fault). Brown to black minerals are biotites (Bt) or 5 hornblendes (Hbl). Greyish large minerals are K-feldpars (Kfs) or plagioclases (Pl). Light grey minerals are micro-fractured quartz (Qz). Red rectangles localize Figure 3b, 3c, 4a, 6, 7 and 8. Yellow arrows indicate breccia-like laumontite-filled veins. b) and c) Microphotographs in plane polarized light (b) and crossed polarized light (c) of a breccia-like laumontite-filled vein showing the angulous mineral fragments within a laumontite matrix. The red dotted lines locate the vein walls.

Solid Earth Discuss., https://doi.org/10.5194/se-2017-130
Manuscript under review for journal Solid Earth
Discussion started: 14 December 2017

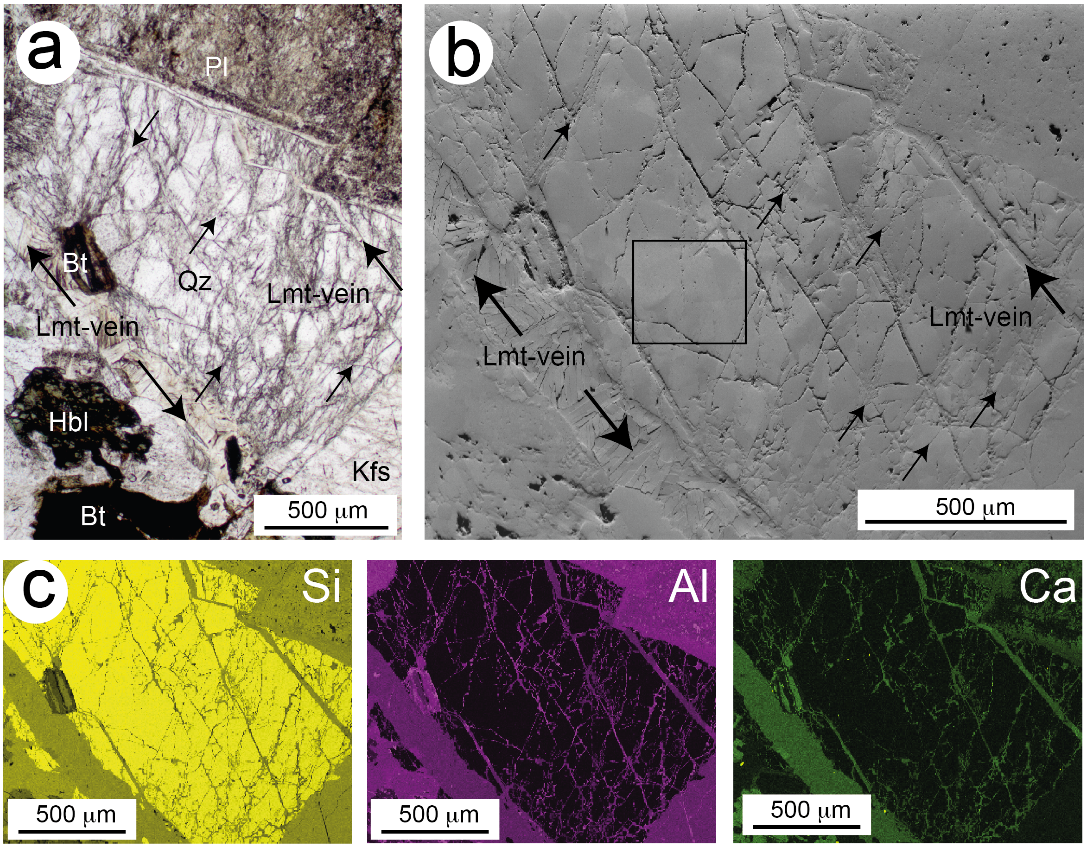

Figure 4 : Representative quartz grain (Qz) studied with EBSD (area shown on Fig. 3a). a) Microphotograph (plane polarized light) of the quartz grain bound by laumontite (Lmt) veins (large black arrows) and surrounded by K-feldspar (Kfs), plagioclase (Pl), biotite (Bt) and hornblende (Hbl). The quartz grain shows abundant well orientated intragranular microfractures (small 5 black arrows). b) Forward-scattered electron image of the same area. Thick arrows : intergranular laumontite-filled veins. Thin arrows : intragranular microfractures and alignments of tiny fluid inclusions. The slightly different grey levels are due to different crystallographic orientations. The rectangle locates the sub-region finely mapped with EBSD (Figure 8) and Laue X-ray microdiffraction (Figure 9). c) Compositional maps of the same area for Si, Ca and Al showing the laumontite-filled veins.

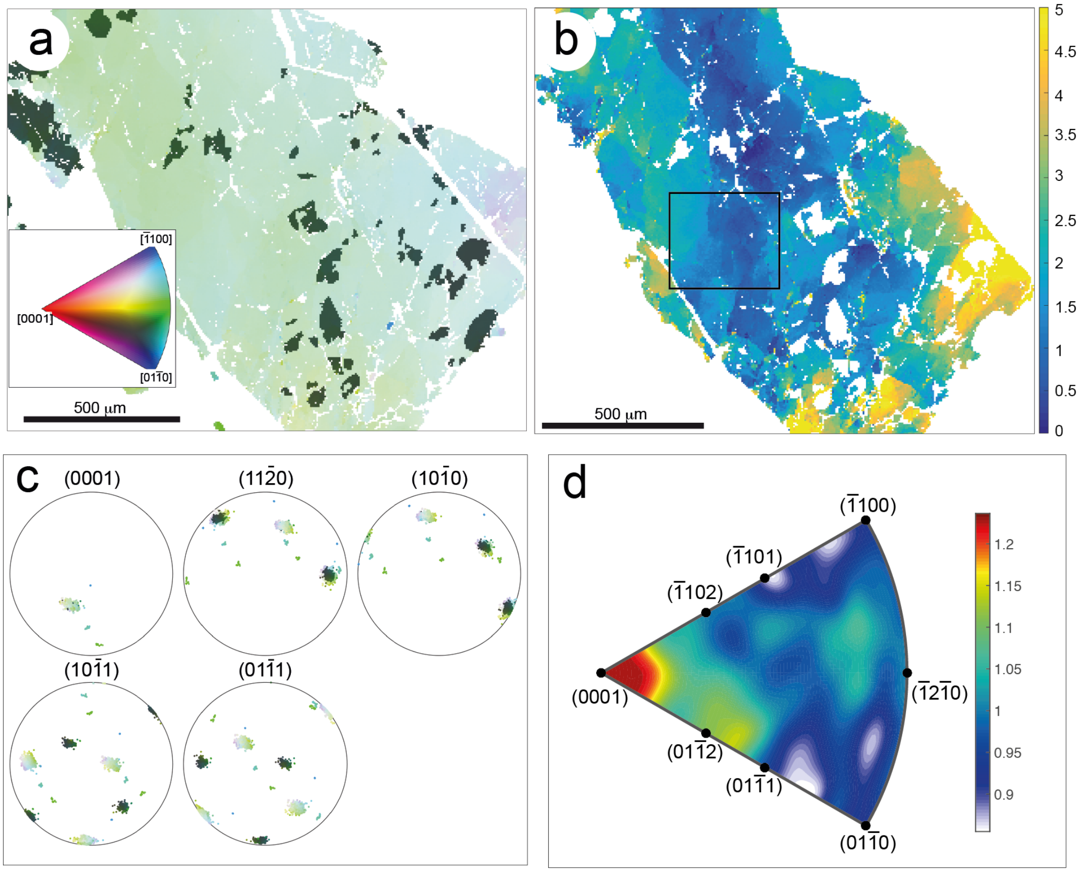

Figure 5 : EBSD measurements on the quartz grain shown in Figure 4. a) Crystallographic orientation map measured by EBSD. The Inverse Pole Figure (IPF) colouring indicates the orientation of each pixel relative to the horizontal axis of the map. The dark green patches correspond to Dauphiné twinned domains defined by a 60° rotation around the [0001] axis. b) Misorientation map relative to the mean orientation of the quartz grain (excluding Dauphiné twins) with misorientations up to 5°. The rectangle indicates the area studied in Figure 10. c) Pole figures of the principal crystallographic axes of quartz using the same colour code as in a). d) Inverse pole figure of rotation axes that correspond to misorientations between 0.5 and 5°. Colour scale : multiple of uniform distribution.

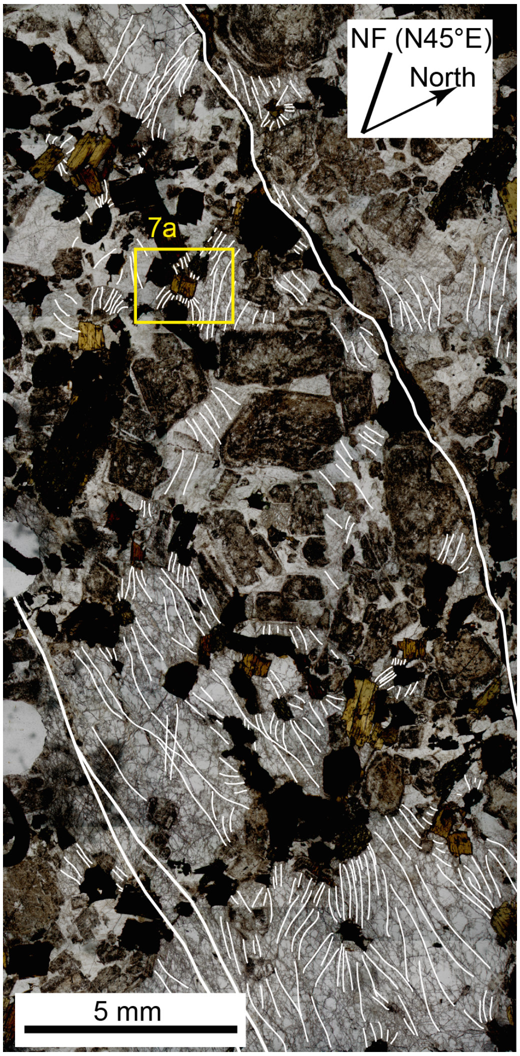

5 **Figure 6 : Schematic drawing on the NOJ220 thin section showing an array of numerous microfractures (thin white lines) joining one biotite or hornblende to another on the entire thin section width. The thicker white line indicates one breccia-like laumontite vein (see Fig. 3a for location). The yellow rectangle localizes the area studied in Figures 7 and 8. The orientation of the thin section is inverse and indicated in the top left box (NF : Nojima fault).**

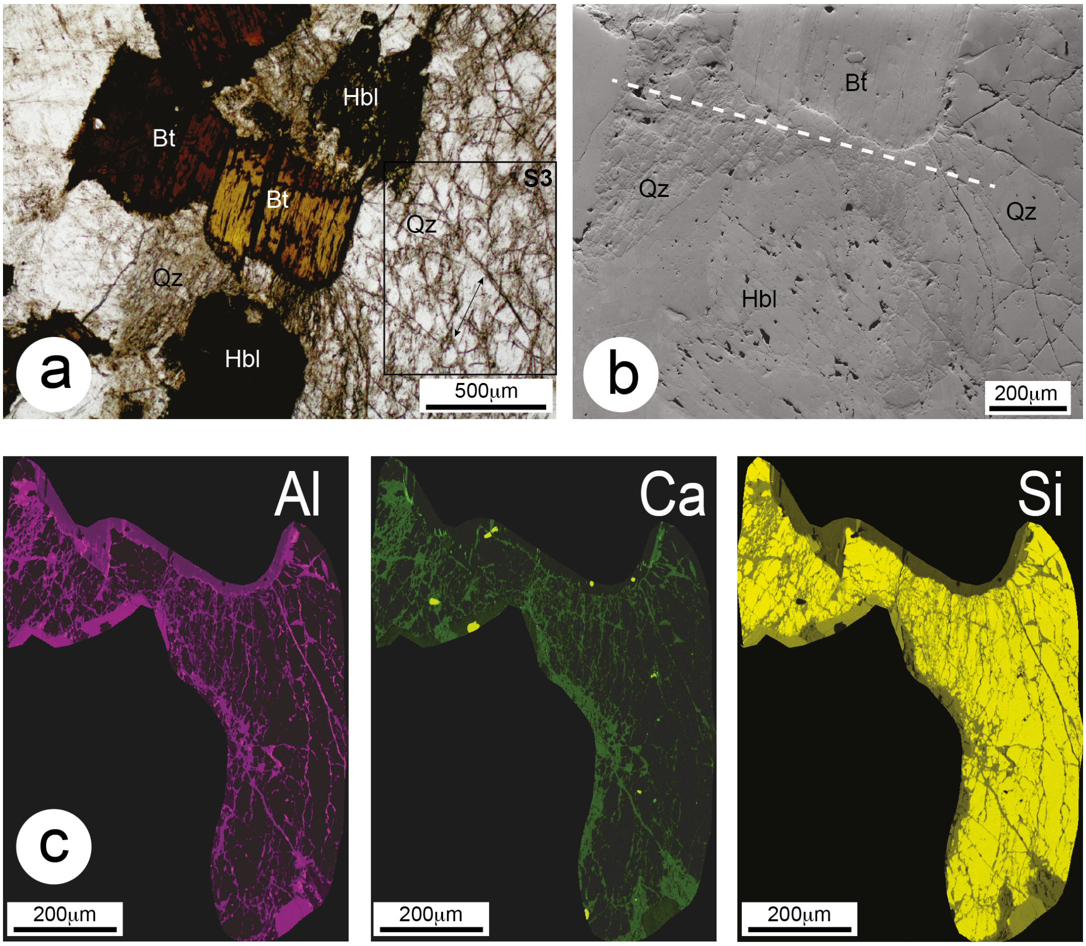

Figure 7 : Microstructures in the area shown in Fig. 3a. a) Quartz grains squeezed between a biotite (Bt) and a hornblende (Hbl) and displaying intensive microfracturing. The small black arrow on the right indicates the preferred orientation of the alignments of tiny fluid inclusions in quartz (compare with Figure 4a). b) Forward-scattered electron image of the same area. The slightly different grey levels in quartz are due to different crystallographic orientations. The white dashed line locates the transect on which a 30% dilatancy has been measured. c) Compositional maps of the same area for Si, Ca and Al showing the laumontite-filled veins.

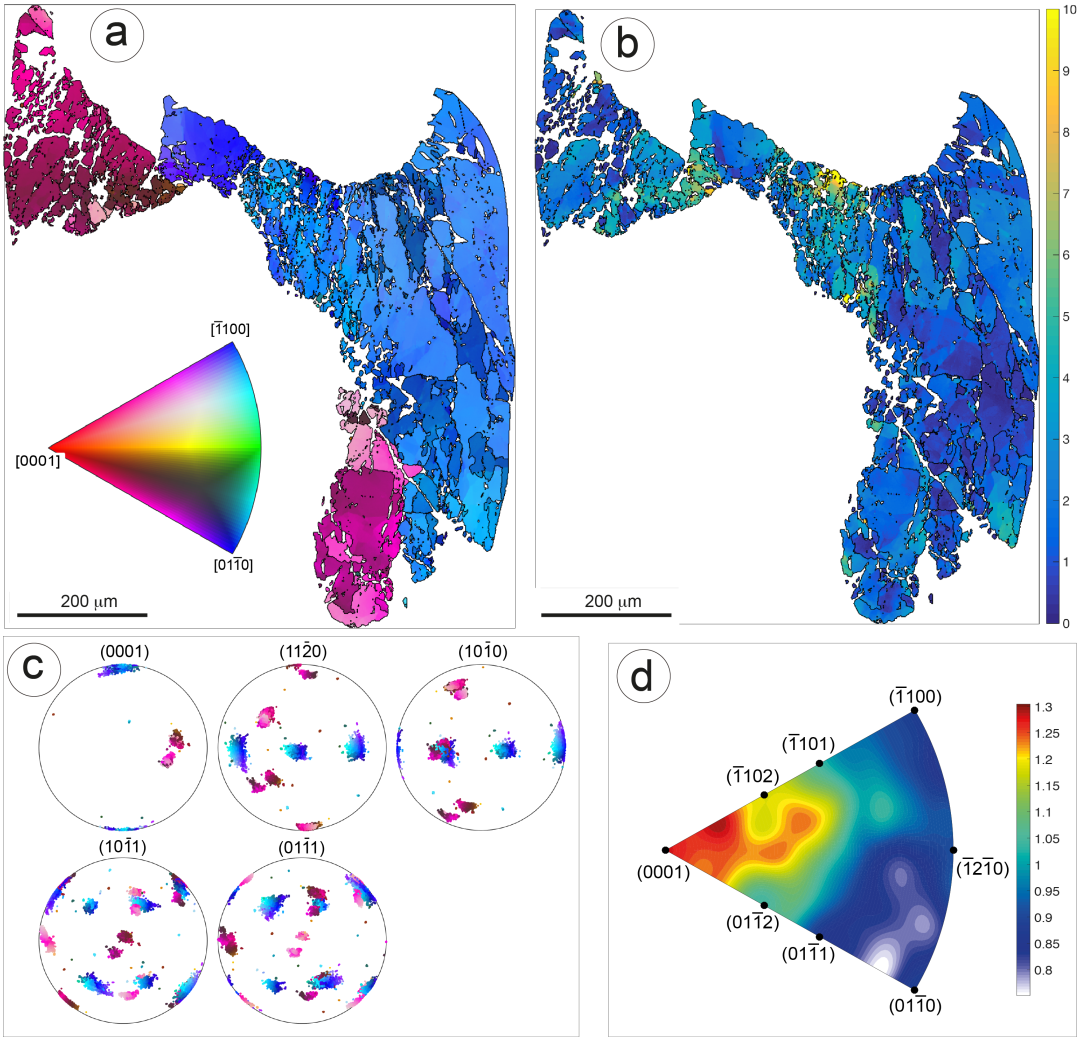

Figure 8 : EBSD measurements on the quartz grains shown in Figure 7. a) Orientation map ; the colour scale indicates the minimum angle between each pixel and the reference orientation defined by (0, 0, 0) Euler angles. b) Misorientation map relative to the mean orientation of each quartz grain with misorientations up to 10°. c) Pole figure of the principal crystallographic axes of the three quartz grains using the same colour code as in a). d) Inverse pole figure of rotation axes that correspond to misorientations between 0.5 and 10°. Colour scale : multiple of uniform distribution.

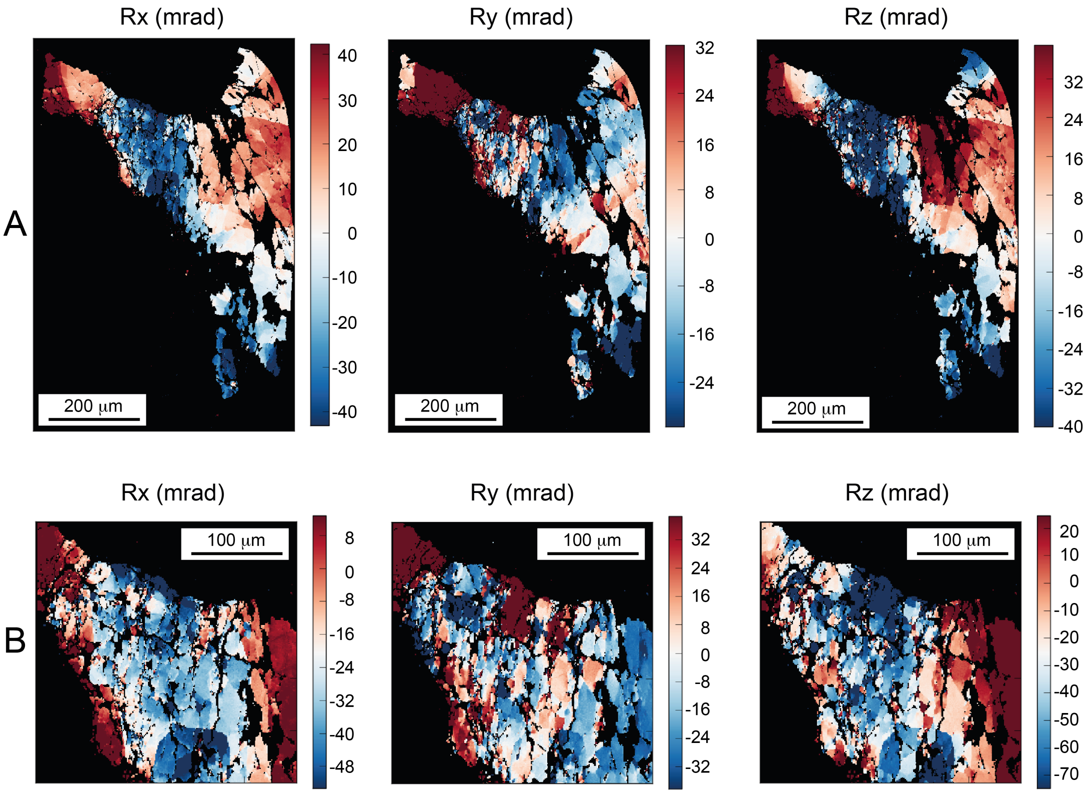

Figure 9 – **Maps of the Rx, Ry and Rz rotations of the crystal lattice around the x, y and z axes (sample referential), in the region explored in Figure 8. Rx, Ry and Rz were calculated with LaueTools from the EBSD data of Figure 8. The x,y map positions and the Euler angles of the EBSD file were first transformed in order to adapt to the LaueTools (LT) reference frames. The corresponding transformations are described in Supplementary Material 4. Histograms of orientation matrix components were then built, for different rectangular regions in the map of figure 8a, in order to identify the frequency peaks associated to the blue crystallite in the center of the map, and to define the thresholds for selecting the map points belonging to this crystallite according to their crystallographic orientation. In figure 9A, all the non-black pixels have their a* vector within less than 245 mrad (14 degrees) of the x axis. These pixels were used to calculate the mean orientation matrix of the crystallite (used as the zero for rotations). The twinned regions appear in black, i.e. they were excluded from the crystallite. A) Rotation components for the right part of Figure 8a. B) Zoom on the top-center area of Figure 8a. Scales in mrad differ (in amplitude and offset) between the different maps, in order to enhance the contrast for each rotation component.**

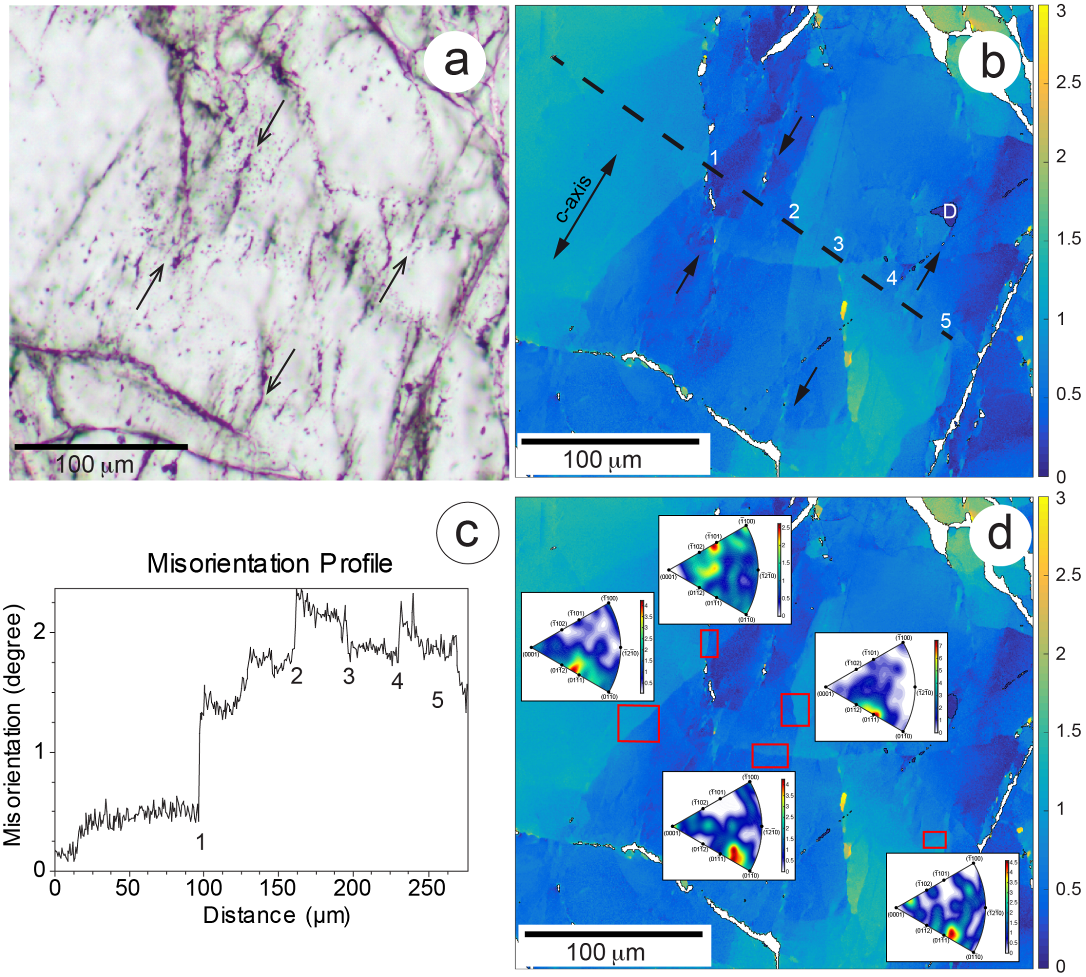

Figure 10 – EBSD measurements on the area shown in Figure 4b. a) Optical microphotograph showing the short microfractures (thin arrows) and alignments of tiny fluid inclusions. b) Map of misorientation of pixels relative to the mean orientation of the grain obtained by EBSD. The small dark domain (D) is a Dauphiné twinned domain. The projection of [0001] axis on the thin section plane is shown by the double black arrow. The short black arrows indicate the well orientated small elongated domains that could correspond to the short wave-length variations between subgrain boundaries or steps indicated as 1 to 5 on profile shown in b. c) Misorientation profile along the dashed line shown in b. d) Misorientation axes calculated for small areas across subgrain boundaries (red rectangles).

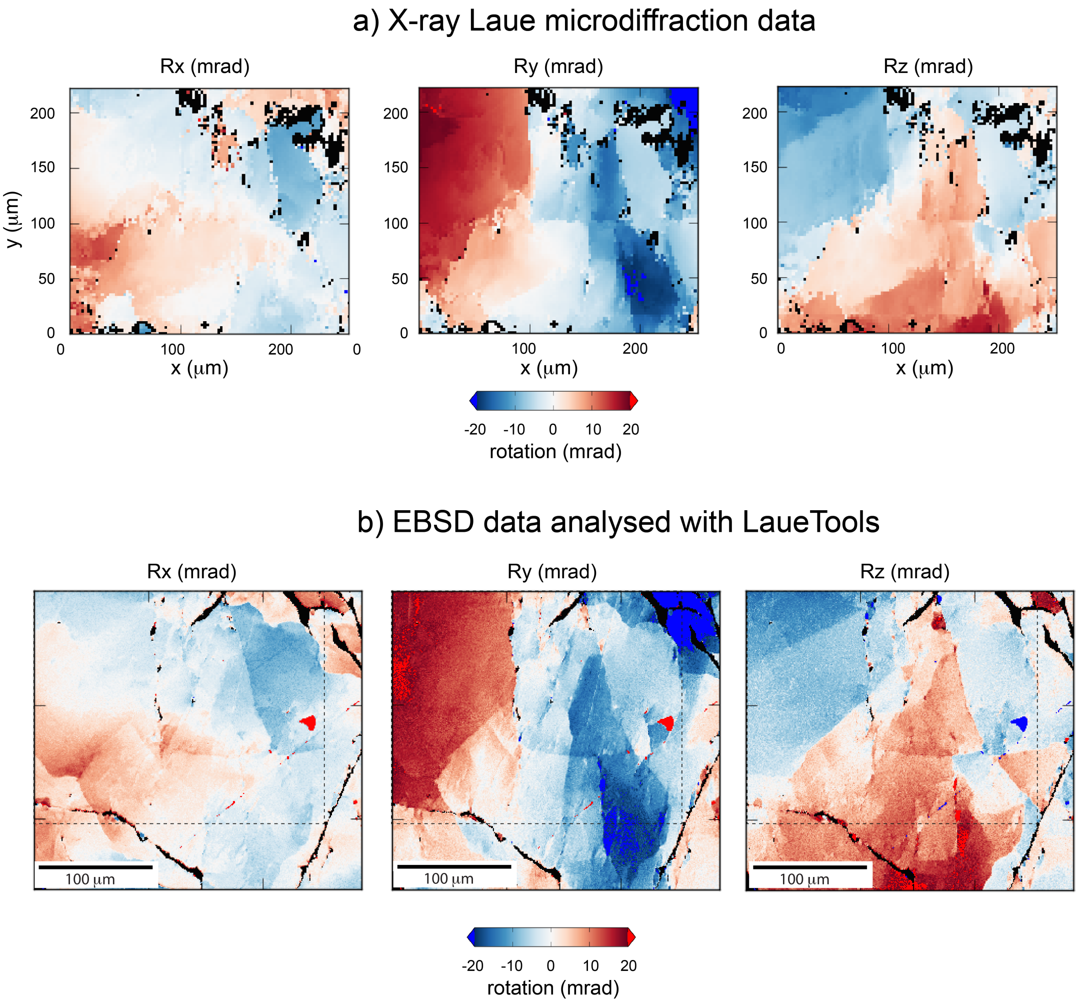

Figure 11 – Maps of the Rx, Ry and Rz rotations of the crystal lattice around the x, y and z axes (sample referential) relative to to the average orientation in each map in the small area described in Figure 10 and calculated using LaueTools. a) Rotations calculated from the X-ray Laue microdiffraction data. b) Rotations calculated from EBSD data. The dashed line indicates the area investigated using X-ray Laue microdiffraction. See Supplementary Material 4 for mathematical transformations applied to the EBSD data in order to pass the orientation matrices and map points positions into the LaueTools sample reference frame. 5

Solid Earth Discuss., https://doi.org/10.5194/se-2017-130
Manuscript under review for journal Solid Earth
Discussion started: 14 December 2017

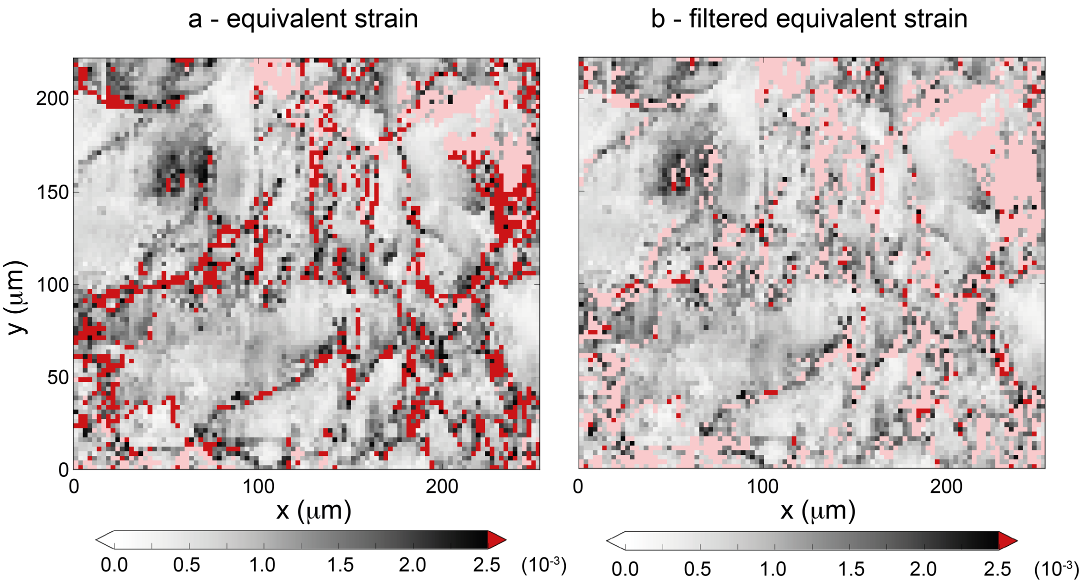

Figure 12 : Maps of the equivalent strain (see formula (1) in the main text) measured from the distorsion between the Laue pattern compared to the theoretical pattern of an undeformed crystal of the same orientation. a) Unfiltered data. Undetermined points are pink. b) Same data after filtering ; same scale as in a, filtered points in pink (7259 images remaining over 8989). Note that filtering eliminates almost all the points showing an equivalent strain greater than 2.5 e^{-3}.

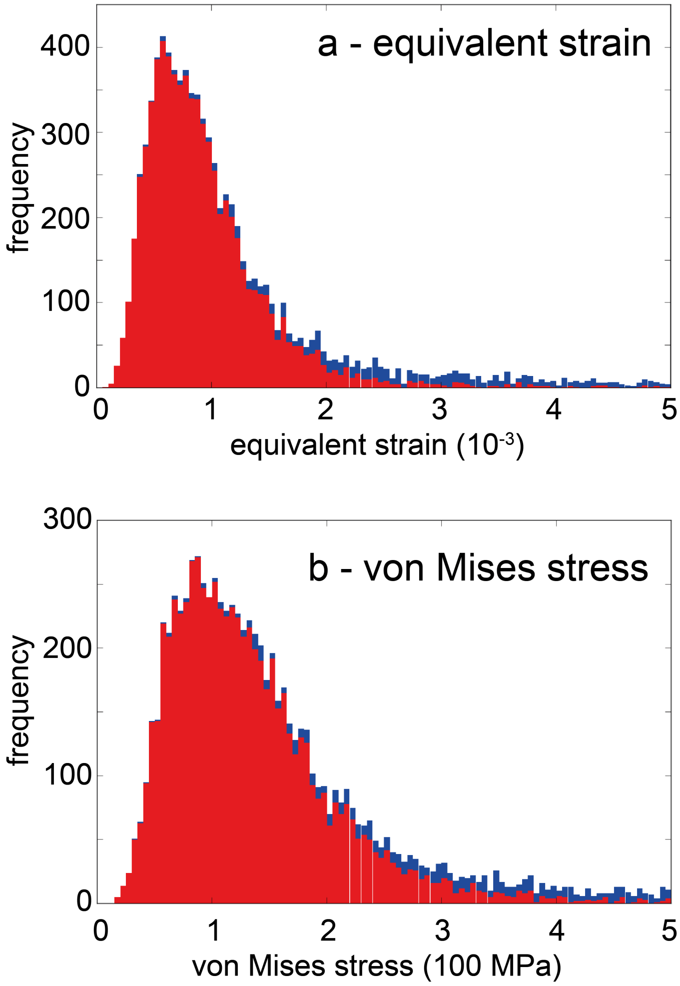

Figure 13 : Distribution histograms of equivalent strain (a) and residual or von Mises stress values (b) without filtering (blue) or with filtering (red).

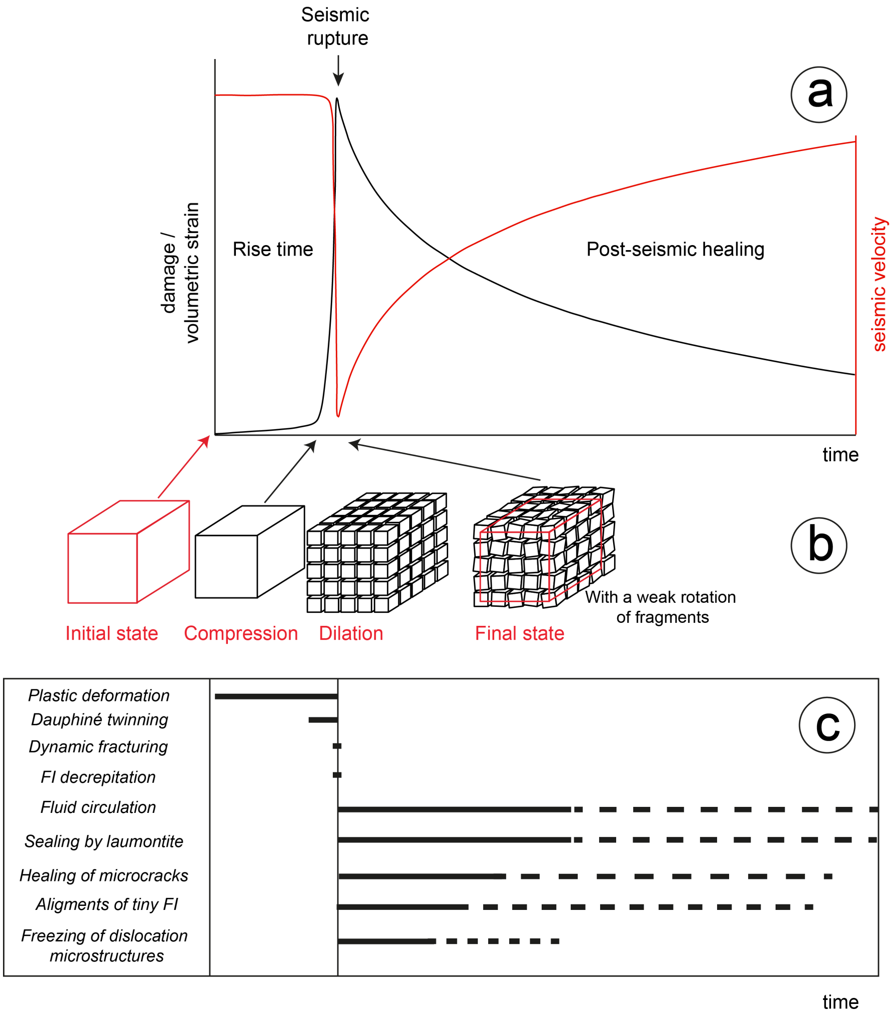

Figure 14 : Schematic interpretation showing the relationships between earthquake and time of formation of the different microstructures observed in the NOJ220 sample. a) Variations of volumetric strain or damage versus time before and after a rupture. The red curve is drawn from the relative velocity changes observed by Brenguier et al. (2008) near Parkfield Parkfield (California) during three years after the M6 9/28/2004 Parkfield earthquake. b) Cartoon inspired by Reches and Dewers (2005) explaining the effect of a rupture front propagating on a fault. Successive compression and dilation (or dilation and compression) leads to fragmentation. c) Time and duration of formation of microstructures relative to the seismic rupture.

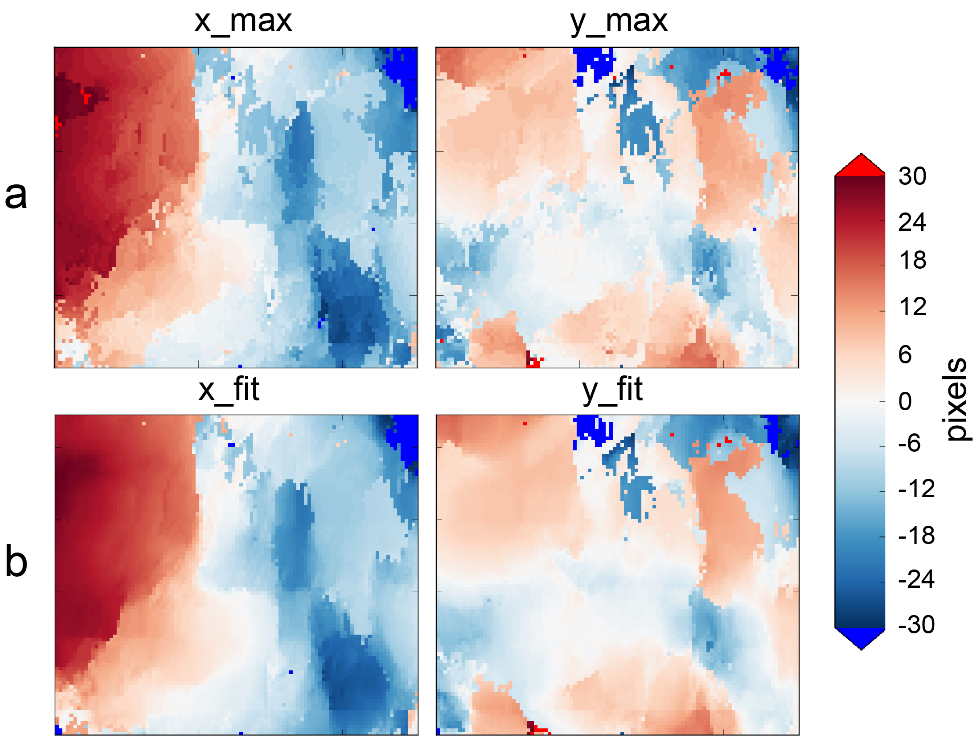

Figure A1 : Laue microdiffraction : one-spot analysis. Maps of the x,y pixel position of the (02-22) spot, for two different methods of calculation of this position. The mean position was subtracted. (a) xy_max (mean = 1476.43, 1211.59), (b) xy_fit (mean = 1476.65, 1211.45). See text of Appendix A for definition. The difference between (a) and (b) is mostly visible for M-type points, where several closely-space sub-grains are present in the beam path.

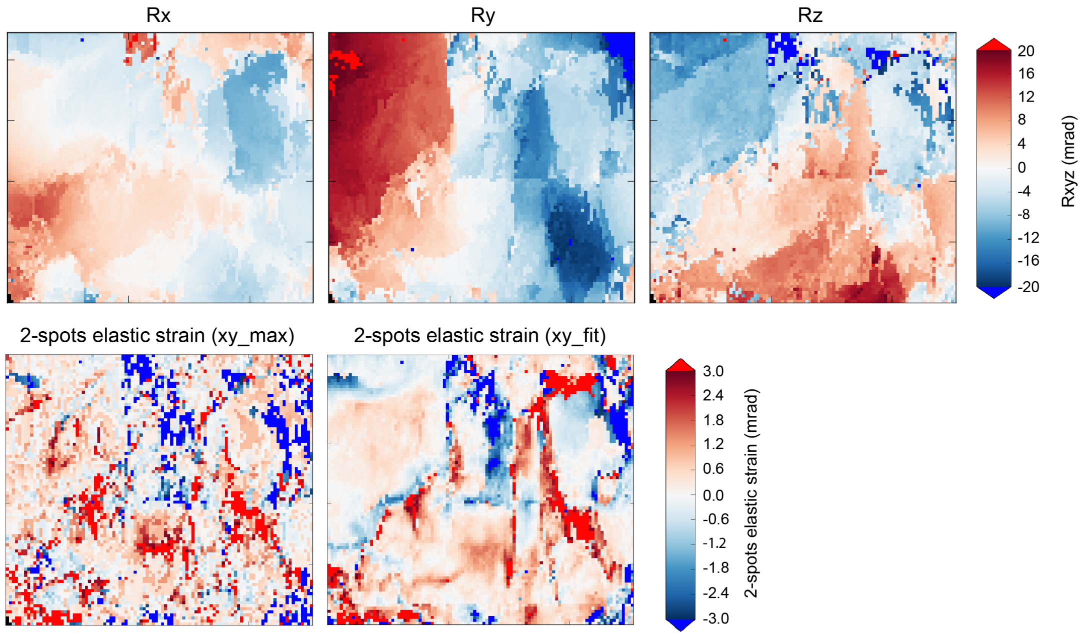

Figure A2 : Maps of three estimators (npeaks, pixdev, and intensity) of the local uncertainty on the shape / orientation of the unit cell, as calculated with the LaueTools software, and final mask used for removing "bad" data points (see explanations in the text). (a) : npeaks : number of Laue spots used for the refinement of the local orientation and deviatoric shape of the quartz unit cell. (b) : pixdev (mean pixel deviation) : estimator of the fit quality. (c) : intensity : average intensity of the 10 most intense spots of the Laue pattern of the grain. (d) : mask used for removing "bad" data points from strain maps, black pixels have npeaks < 25 or pixdev > 1. Pink points in Figure A2 a, b, c are points where the spot-link failed (missing points), and black points of the mask correspond to points either missing or with a npeaks below 25 or a mean pixdev above 1 pixel.

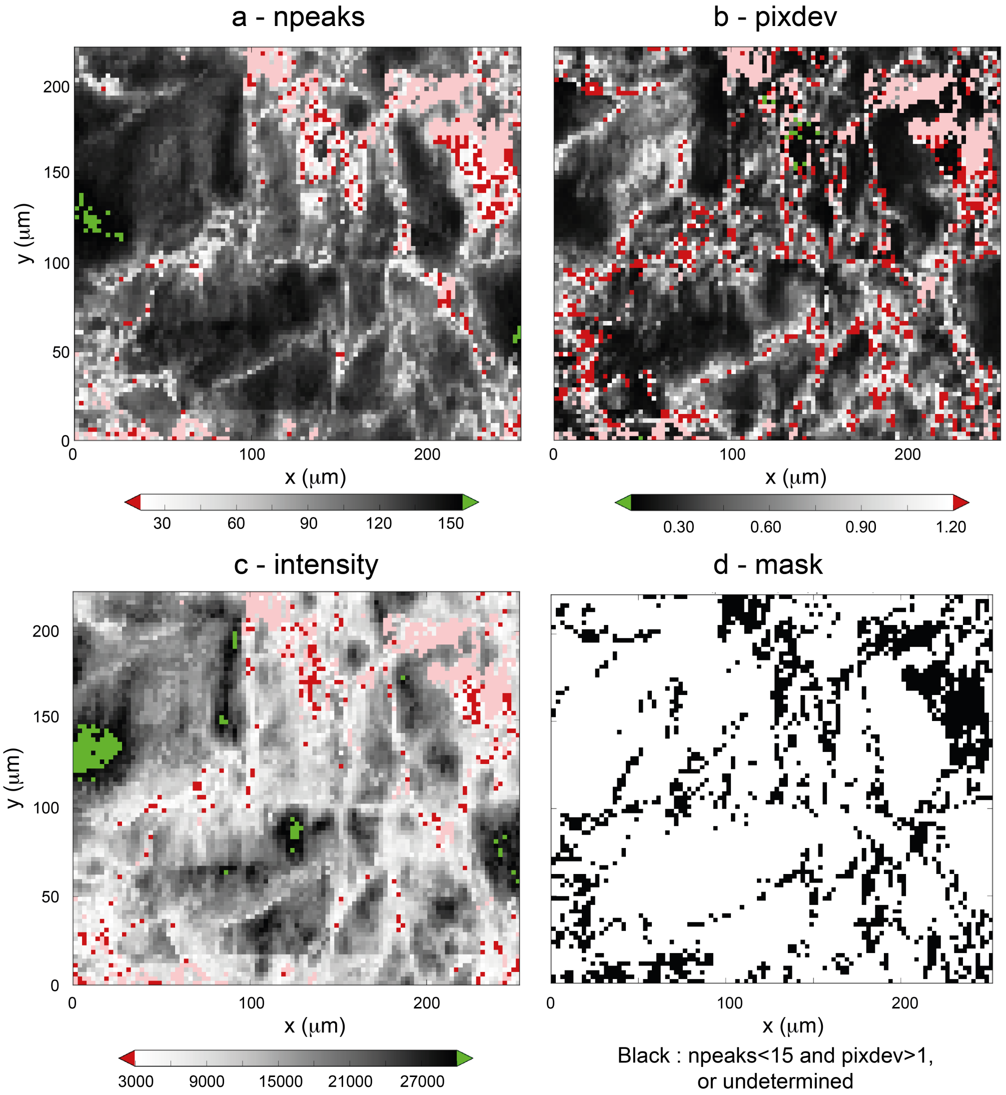

5 **Figure A3 : Laue microdiffraction : two-spots analysis, using the xy_max position of the (02-22) and (-2203) spots. (a) lattice rotations with respect to the mean orientation, around the axes of the sample reference frame. (b) 2 spots elastic strain as measured from the angle between the reciprocal lattice vectors of the two spots (after subtracting the angle for unstrained quartz). (c) same as (b) using xy_fit. High strain map points (dalf > 5 mrad) are excluded when calculating the mean orientation matrix used in (a).**